

Gas and Dust Properties in the Chamaeleon Molecular Cloud Complex based on the Optically Thick H I

K. HAYASHI,¹ R. OKAMOTO,¹ H. YAMAMOTO,¹ T. HAYAKAWA,¹ K. TACHIHARA,¹ AND Y. FUKUI^{2,1}

¹*Department of Physics, Nagoya University, Furo-cho, Chikusa-ku, Nagoya 464-8601, Japan*

²*Institute for Advanced Research, Nagoya University, Furo-cho, Chikusa-ku, Nagoya 464-8601, Japan; sano@a.phys.nagoya-u.ac.jp*

(Accepted May 8, 2019)

ABSTRACT

Gas and dust properties in the Chamaeleon molecular cloud complex have been investigated with emission lines from atomic hydrogen (H I) and ¹²CO molecule, dust optical depth at 353 GHz (τ_{353}), and *J*-band infrared extinction (A_J). We have found a scatter correlation between the H I integrated intensity ($W_{\text{H I}}$) and τ_{353} in the Chamaeleon region. The scattering has been examined in terms of possible large optical depth in H I emission ($\tau_{\text{H I}}$) using a total column density (N_{H}) model based on τ_{353} . A nonlinear relation of τ_{353} with the ~ 1.2 power of A_J has been found in opaque regions ($A_J \gtrsim 0.3$ mag), which may indicate dust evolution effect. If we apply this nonlinear relation to the N_{H} model (i.e., $N_{\text{H}} \propto \tau_{353}^{1/1.2}$) allowing arbitrary $\tau_{\text{H I}}$, the model curve reproduces well the $W_{\text{H I}}-\tau_{353}$ scatter correlation, suggesting optically thick H I ($\tau_{\text{H I}} \sim 1.3$) extended around the molecular clouds. Based on the correlations between the CO integrated intensity and the N_{H} model, we have then derived the CO-to-H₂ conversion factor (X_{CO}) on $\sim 1.5^\circ$ scales (corresponding to ~ 4 persec) and found spatial variations of $X_{\text{CO}} \sim (0.5-3) \times 10^{20} \text{ cm}^{-2} \text{ K}^{-1} \text{ km}^{-1} \text{ s}$ across the cloud complex, possibly depending on the radiation field inside or surrounding the molecular clouds. These gas properties found in the Chamaeleon region are discussed through a comparison with other local molecular cloud complexes.

Keywords: ISM: atoms — ISM: individual objects (Chamaeleon Molecular Cloud) — ISM: molecules

1. INTRODUCTION

The neutral hydrogen on the atomic and molecular forms occupies major mass of the interstellar medium (ISM) and is a fundamental constituent of the ISM. In the electronic ground state neutral atomic hydrogen (H I) has two spin states where the spin angular momenta of a proton and an electron are parallel or anti-parallel. The energy separation between the two states is small (5.9×10^{-6} eV) and corresponds to a wavelength of 21 cm. The 21 cm H I transition is used to calculate H I column density ($N_{\text{H I}}$) usually by assuming that the emission is completely optically thin (e.g., Boulanger & Perault 1988).

The interstellar H I gas, however, has density and temperature which range over order of magnitude: density is distributed from 1 cm^{-3} to 10^3 cm^{-3} and temperature from 10 K to 10^4 K (e.g., Draine 2011). The gas consists of two distinct phases, the cold neutral medium (CNM) and the warm neutral medium (WNM). The CNM is dense and cool ($\sim 30 \text{ cm}^{-3}$ and ~ 60 K), while the WNM is diffuse and warm ($\sim 0.6 \text{ cm}^{-3}$ and ~ 2000 K) (e.g., Heiles & Troland 2003b; Draine 2011). The H I gas is highly turbulent and transient because it is continuously shocked by supernovae every million year.

To measure precisely the local H I gas with the large variations of the optical depth, Fukui et al. (2014, 2015) (hereafter F14, F15) proposed a method to calculate $N_{\text{H I}}$ based on dust optical depth at 353 GHz (τ_{353}), which is estimated from modified black body spectra fitted to the fluxes at submillimeter wavelengths measured by the *Planck* and *IRAS* satellites (Planck Collaboration 2014a). τ_{353} is measured to be very small in the order of $\sim 10^{-3}$, toward the Galactic mid plane and we are able to use τ_{353} as a tracer of $N_{\text{H I}}$ if the gas to dust ratio is uniform. The results of F14 and F15 give a suggestion that the H I emission can be optically thick in the order of 1.0 with low spin temperature ($T_s \lesssim 100$ K) and the considerable amount of atomic hydrogen is underestimated by the optically thin assumption often adopted in studies of the local ISM.

Stanimirović et al. (2014) carried out H I absorption observations toward 26 radio continuum sources behind Perseus using the Arecibo 305 m telescope. These authors showed that the H I optical depth (τ_{HI}) in the emission-absorption measurements is significantly smaller than that derived by F14 and F15; the peak optical depth of $\tau_{\text{HI}} > 0.5$ for only 21 out of 107 individual Gaussian components, as opposed to F14 who found $\tau_{\text{HI}} > 0.5$ for 85% of lines of sight at high Galactic latitudes. The results by Stanimirović et al. (2014) are consistent with those by Heiles & Troland (2003a,b) toward 79 extragalactic sources and raised a question on F14 and F15.

Recently, Fukui et al. (2018) made synthetic observations of 21 cm emission and absorption by using the magneto-hydrodynamic simulations performed by Inoue & Inutsuka (2012) and presented that the synthetic observations are consistent with the optically thick H I and the T_s -dependent relationship between N_{HI} and the H I integrated intensity (W_{HI}) suggested by F14 and F15. In addition, Fukui et al. (2018) found that the WNM with $\tau_{\text{HI}} < 0.5$ and with T_s higher than 300 K is extended by $\sim 70\%$ in the sky and the radio absorption toward extragalactic continuum sources is biased toward WNM. These results give an estimate that the optically thin approximation for the H I emission underestimates the H I mass by a factor of ~ 1.3 . Okamoto et al. (2017) showed that the H I distribution in the Perseus molecular cloud can be reproduced well by the total column density (N_{H}) model as a function of $\sim 1/1.3$ th power of τ_{353} . The authors derived that the H I column density is 1.6 times higher than that of the optically thin case, suggesting that a large amount of the optically thick H I around the molecular clouds. The nonlinear behavior between τ_{353} and N_{H} indicates dust evolution effect, as suggested from measurements of dust opacity in local molecular clouds (e.g., Roy et al. (2013) for Orion A molecular cloud).

Among other local molecular cloud complex, the Chamaeleon complex is known as a nearby low-mass star-forming region at a distance of ~ 150 pc, whose molecular cloud mass is estimated to be $\sim 5000\text{--}8300 M_{\odot}$ (e.g., Mizuno et al. 2001; Ackermann et al. 2012; Planck Collaboration 2015). The cloud properties and the moderate star formation activities are reviewed by Luhman (2008). Planck Collaboration (2015) attempted to model the gas distribution in the Chamaeleon region with a linear combination of H I, CO and “dark gas”, a neutral gas component that cannot be traced by standard H I and CO observations, and estimated the gas column density by fitting these gas model maps to γ -rays and thermal dust emission models (dust extinction, τ_{353} and radiance). The dark gas template is constructed through iterating fittings to the γ -rays and dust data alternately. T_s in H I emission is assumed to be uniform and the optically thin approximation is adopted because it gives a better fit to the γ -ray data as compared to other H I maps with several uniform T_s from 125 K to 800 K. Although gas properties in the cloud complex are discussed under the assumption of CO-dark H_2 (e.g., Wolfire et al. 2010; Smith et al. 2014) as a candidate of the dark gas, quantitatively estimate of the optically thick H I is not performed in their studies. The assumption of a uniform T_s makes difficult to examine the H I gas with low T_s present in the CNM (e.g., Heiles & Troland 2003b).

On the other hand, F14 and F15 have attempted to examine a total column density model as a function of τ_{353} . The N_{H} model not relying on a uniform T_s allows accurate measurements of the H I gas. F14 and F15 found that the N_{H} model reproduces the scatter correlation in the $\tau_{353}\text{--}W_{\text{HI}}$ relationship, suggesting a large amount of the optically thick H I around molecular clouds. Okamoto et al. (2017) demonstrated that the N_{H} model is applicable in the Perseus molecular clouds and suggested the average H I optical depth is up to ~ 0.9 . Using the obtained N_{H} model, the authors also derived a spatial distribution of the CO-to- H_2 conversion factor (X_{CO}) with the average value $\sim 1.0 \times 10^{20} \text{ cm}^{-2} \text{ K}^{-1} \text{ km}^{-1} \text{ s}$, which is comparable to past measurements of the Galactic interstellar clouds (e.g., Bolatto et al. 2013).

In this paper, we aim to investigate gas properties in the Chamaeleon region, focusing on the optically thick H I, by attempting the method applied in Okamoto et al. (2017). The aim of the present paper is summarized below.

- Applying the τ_{353} -based N_{H} model to the Chamaeleon complex and to understand the physical states of the H I gas through a comparison with F14 (MBM 53, 54, 55 and HLC G9235, hereafter denote as MBM 53–55), F15 ($|b| > 15^\circ$ in the all sky), and Okamoto et al. (2017) (Perseus) and derive the distribution of an X_{CO} factor.
- To test dust evolution found in the Orion A (Roy et al. 2013) and the Perseus (Okamoto et al. 2017) regions. This will bring a better understanding of dust properties in the local ISM.

This paper is organized as follows. Section 2 shows observational datasets. Section 3 summarizes gas properties in the Chamaeleon region. Section 4 describes the N_{H} model applied in this study. In Section 5, we discuss possibility of the optically thick H I and these gas properties in comparison with other local molecular clouds. A summary is given in Section 6. All velocity information in the present paper is represented by local standard of rest (denoted as V_{LSR}).

2. OBSERVATIONAL DATASETS

To investigate gas and dust properties in the Chamaeleon region, we have used the following datasets.

2.1. *H I Data*

The Galactic All-Sky Survey (GASS) conducted with the Parkes 64 m radio telescope has provided the most sensitive and the highest resolution data of the H I 21 cm line emission for the southern sky (McClure-Griffiths et al. 2009; Kalberla et al. 2010; Kalberla & Haud 2015). In this study, we have used the second released GASS data¹, in which effects of stray radiation received by the antenna diagram have been corrected (Kalberla et al. 2010). We have kept HPBW 16' and the velocity resolution 0.82 km s⁻¹ in the original data. A typical noise level for the analysis region in root-mean-square (rms) is ~ 0.05 K per channel. The measured velocity range for the Chamaeleon region is -500 km s⁻¹ to $+400$ km s⁻¹, but most of the H I line velocities span -40 km s⁻¹ $\lesssim V_{\text{LSR}} \lesssim +20$ km s⁻¹ except for possible contribution from the Large Magellanic Cloud (LMC) at $+200$ km s⁻¹ $\lesssim V_{\text{LSR}} \lesssim +300$ km s⁻¹.

2.2. *CO Data*

To trace the distribution of molecular hydrogen, we have used ¹²CO $J=1-0$ emission line observed by the NANTEN 4 m millimeter telescope located at Las Campanas, Chile. NANTEN observations toward the Chamaeleon region were performed during two periods, from July to September in 1999 and from October to December in 2000 (Mizuno et al. 2001). The HPBW of the data is 2'6 at 115 GHz with grid spacing of 8' and typical noise fluctuation is ~ 0.3 K at a velocity resolution of 0.1 km s⁻¹.

2.3. *Planck and IRAS Dust Emission Data*

The *IRAS* and *Planck* satellites performed the all-sky survey in millimeter/submillimeter wavelength, providing high-quality data of the thermal dust emission. The measured intensities of the *Planck* 353, 545, and 857 GHz data and of the IRIS (Improved Reprocessing of the *IRAS* Survey) 100 μ m data were fitted by modified-blackbody intensity spectra (Planck Collaboration 2011b), which reveals dust properties down to 5' spatial resolution in HPBW with relative accuracy of $\sim 10\%$. In this analysis, we have used the dust optical depth at 353 GHz (τ_{353}) and the dust temperature (T_d) to model/evaluate the total gas column density. The data with HEALPix format (Górski et al. 2005) released version R1.10² are used.

2.4. *J-band Extinction Data*

Using the 2MASS (two micron all-sky survey) infrared extinction data measured at J , H , and K bands, Juvela & Montillaud (2016) have derived interstellar extinction map at the J band (A_J) over the whole sky, with optimal techniques to map the dust column density ("NICER"; Lombardi & Alves 2001 and "NICEST"; Lombardi 2009). In the present study, we have used the A_J map constructed with the "NICEST" method to investigate correlation with the dust optical depth for the Chamaeleon complex. An all-sky map given in magnitude at the spatial resolution 3' (full width half maximum) with the HEALPix format was downloaded from the archival page³. The typical noise fluctuation for the Chamaeleon region is ~ 0.08 mag in rms.

2.5. *H α Data*

We have used the optical H α data obtained by Finkbeiner (2003) in order to identify the bright H II regions, where dust grains are heated up or destroyed by ultraviolet (UV) radiation and the neutral hydrogen is ionized as well. In the present study, these regions are masked to avoid mixing different gas properties in local specific environment (e.g., faint diffuse gas exposed by the strong radiation near the Galactic plane). The typical sensitivity for the Chamaeleon region is estimated to be ~ 0.3 R and the spatial resolution is 6' in HPBW.

2.6. *21 cm Radio Continuum Data*

Radio continuum data have been used to estimate contribution from the background radiation, including the 2.7 K cosmic microwave background. We have used the 21 cm (1.4 GHz) "CHIPASS" continuum map (Calabretta et al.

¹ The H I 4 π (HI4PI) survey (Bekhti et al. 2016) adopting the third revision of GASS data (Kalberla & Haud 2015) were released in 2016. Instrumental effects remained in the past GASS data are corrected. We confirmed that our results do not change significantly even if we use these revised data.

² http://irsa.ipac.caltech.edu/data/Planck/release_1/all-sky-maps/

³ <http://www.interstellarmedium.org>

2014), which have been constructed by a combination of H I data obtained from the Parkes All-Sky Survey and Zone of Avoidance survey. The typical sensitivity is ~ 40 mK and the spatial resolution is $14''.4$ in HPBW.

3. GAS AND DUST PROPERTIES IN CHAMAELEON REGION

3.1. Gas and Dust Spatial Distributions

Using the datasets described in Section 2, we have made maps showing spatial distributions of the gas and dust properties in the Chamaeleon region, which are summarized in Figure 1. Each map on the panels (a)–(h) are described below.

- (a) Velocity-integrated intensity map of the $^{12}\text{CO } J=1-0$ line (hereafter denoted as W_{CO}) obtained by the NANTEN 4 m telescope. The integrated velocity range is from -16 km s^{-1} to $+16 \text{ km s}^{-1}$, where most of the emission is included. The peak intensity in $W_{\text{CO}} \sim 25 \text{ K km s}^{-1}$ is intermediate between those measured from the MBM 53–55 (Yamamoto et al. 2003) and Perseus (Okamoto et al. 2017) molecular clouds.
- (b) Velocity-integrated intensity map of the H I 21 cm line (W_{HI}) obtained from the GASS data (McClure-Griffiths et al. 2009; Kalberla et al. 2010). The integrated velocity range is from -500 km s^{-1} to $+400 \text{ km s}^{-1}$ in the original data. Although scanning effects are found in $300^\circ \lesssim l \lesssim 310^\circ$, $-20^\circ \lesssim b \lesssim -12^\circ$ (see also Figure 8 in Kalberla & Haud 2015), we confirmed that they do not affect the result of this study. The gas along the line of sight within the region is mainly separated into three components on the basis of the velocity line profile (see Section 3.3).
- (c) τ_{353} map obtained from the thermal dust emission model based on the *Planck*/*IRAS* data.
- (d) Dust temperature map obtained from the thermal dust emission model based on the *Planck*/*IRAS* data.
- (e) J -band extinction (A_J) (Juvela & Montillaud 2016) obtained with “NICEST” method (Lombardi & Alves 2001) using the 2MASS near infrared data.
- (f) $\text{H}\alpha$ intensity map to search the H II regions.
- (g) Brightness temperature at 21 cm wavelength derived by Calabretta et al. (2014). The map has been used to estimate the background brightness temperature at 21 cm (T_{bg}) (see Section 4).

3.2. Masking Areas

In the present study, when focusing on the atomic gas data, we have masked the molecular gas regions to remove data points with possible contamination from the high-density regions. We also applied the mask to several areas having velocity profiles different from the local clouds with the peaks at $V_{\text{LSR}} \sim 0 \text{ km s}^{-1}$ (see also Section 3.3) and regions heated by the interstellar radiation field (ISRF), which may change the local gas-to-dust ratio. The areas including the LMC components are also masked, since their gas-to-dust ratio are much different from the local ISM. Figures 2(a)–(f) show the masked regions applied in this analysis.

- (a) The areas with significant CO emission ($W_{\text{CO}} > 1.2 \text{ K km s}^{-1}$ ($\sim 3 \sigma$)), where H_2 is dominant compared to H I.
- (b) Intermediate-velocity clouds (IVCs) observed in the negative velocity range. The areas with $W_{\text{HI}} > 50 \text{ K km s}^{-1}$ at $V_{\text{LSR}} < -30 \text{ km s}^{-1}$ are masked.
- (c) The areas including outskirts and streams around the LMC, which are seen around the bottom-right part in the analysis region (see the gas and dust distributions in Figures 1(b)–(g)).
- (d) Intermediate-velocity arc (IVA) consisting of H I-dominated clouds characterized by an elongated gas structure across the whole longitude direction at $-15 \text{ km s}^{-1} \lesssim V_{\text{LSR}} \lesssim -5 \text{ km s}^{-1}$ (Planck Collaboration 2015). We masked areas where the contribution from IVA is more dominant ($l < 290^\circ$ and $b < -22^\circ$) compared to the local H I clouds (see details in Section 3.3).
- (e) The position around a Be star HIP 70248 located at $(l, b) \sim (306^\circ.9, -18^\circ.0)$

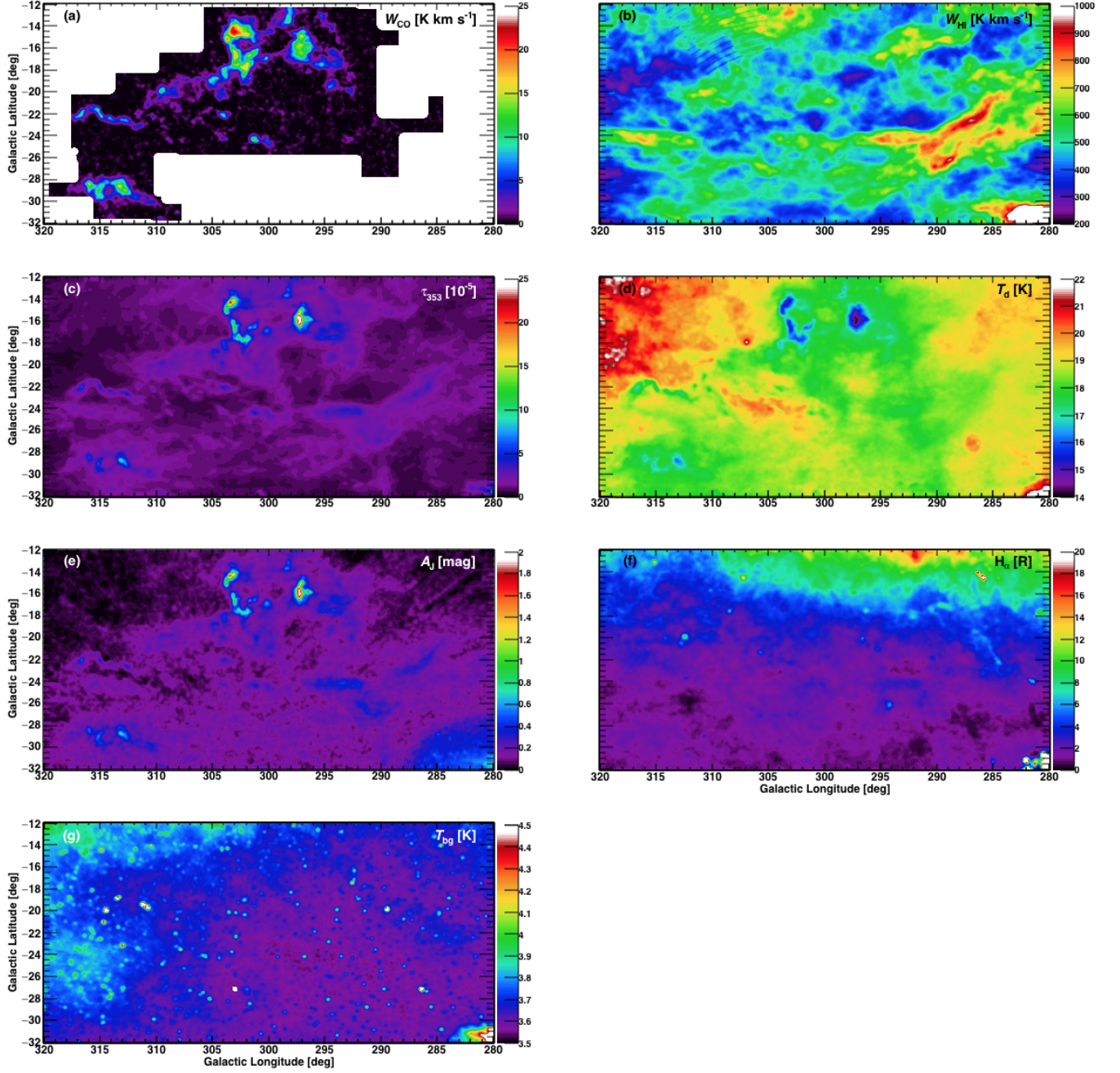


Figure 1. Spatial distributions of the gas and dust properties in the Chamaeleon region corrected for the $16'$ effective beam size: (a) W_{CO} obtained with the NANTEN telescope. (b) W_{HI} from the GASS data. (c) τ_{353} and (d) T_d based on the *Planck/IRAS* observations. (e) A_J obtained through the NICEST method using the 2MASS data. (f) $\text{H}\alpha$ intensity map from Finkbeiner (2003). (g) 21 cm radio continuum map (Calabretta et al. 2014). Details are described in the text.

(f) The region with $\text{H}\alpha > 10 \text{ R}$, where the dust grains are heated up or destroyed and hydrogen gas is ionized.

The mask (a) is applied to Figures 5(a), 7, 9(a), 10 (except for the N_{H} histogram in the panel (c)), 15(c) and 18. The other masks are applied to Figures 4–11, 13, 15(c) and 19.

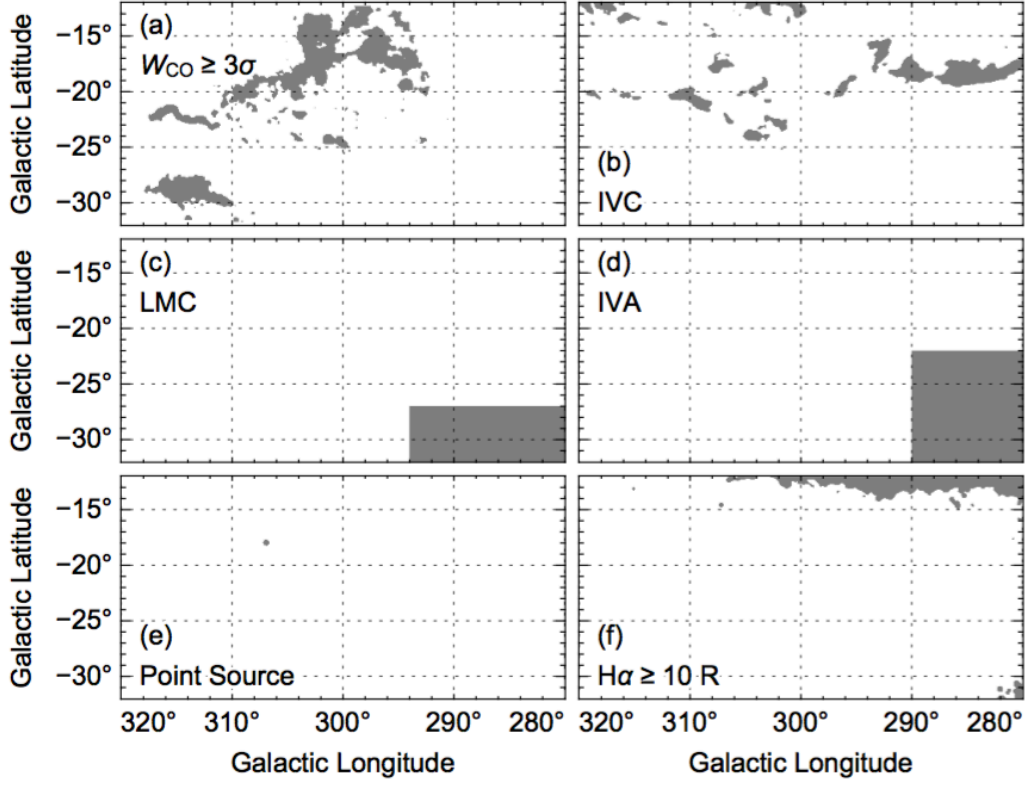


Figure 2. Masked areas (shown by the shaded color) applied in the present analysis: (a) molecular gas with $W_{\text{CO}} > 3\sigma$. (b) IVCs with $W_{\text{HI}} > 50 \text{ K km s}^{-1}$ at $V_{\text{LSR}} < -30 \text{ km s}^{-1}$. (c) LMC- and (d) IVA-dominated regions. (e) Position of a Be star, HIP 70248. (f) Ionized gas with $\text{H}\alpha > 10 \text{ R}$. Details are described in the text.

3.3. Velocity Structure in the Neutral Gas

Line profiles obtained from the H I and CO data allow kinematical separations of the gas distribution. Figure 3(a) indicates an H I intensity spectrum showing the brightness temperature ($T_{\text{H I}}$) averaged in the analysis region. Figure 3(b) is an average longitude-velocity diagram, which overlays the CO intensity represented by the black contours. We have found three components separated by the dashed vertical lines in the spectrum, whose gas structures are seen in the longitude-velocity diagram and a velocity channel map shown in Figure 16: (i) local clouds with the intensity peak around $V_{\text{LSR}} = 0 \text{ km s}^{-1}$, at which most of the CO emission is detected; (ii) wing-like structure at the intermediate velocity range spanning $-15 \text{ km s}^{-1} \lesssim V_{\text{LSR}} \lesssim -5 \text{ km s}^{-1}$, which corresponds to the IVA (Planck Collaboration 2015) characterized by a mild gradient in the velocity toward the negative longitude direction, with comparatively bright H I emission at $280^\circ \lesssim l \lesssim 290^\circ$; (iii) high velocity component with a long tail at $V_{\text{LSR}} \lesssim -20 \text{ km s}^{-1}$, which corresponds to faint diffuse emission observed at $302^\circ \lesssim l \lesssim 314^\circ$, exhibiting bridging feature connected to the intermediate clouds. To more clearly show that the H I spectrum can be separated into the three components, we give examples of the spectra in Figure 17 for restricted regions with the size of $1^\circ \times 1^\circ$. Planck Collaboration (2015) also shows that the similar spectral separation can be applied in the Chamaeleon region. In order to remove contamination from clouds other than the local Chamaeleon complex, we have masked the region at $(280^\circ \leq l \leq 290^\circ, b \leq -22^\circ)$, where contribution from the IVA is relatively large, and the regions with strong emission from the high velocity component. Although the IVA component is extended toward $l \gtrsim 290^\circ$, from which the faint diffuse emission at the high velocity range is observed, these contributions are not significant compared to that from the local H I clouds lying at the same line of sight. We therefore do not mask this area.

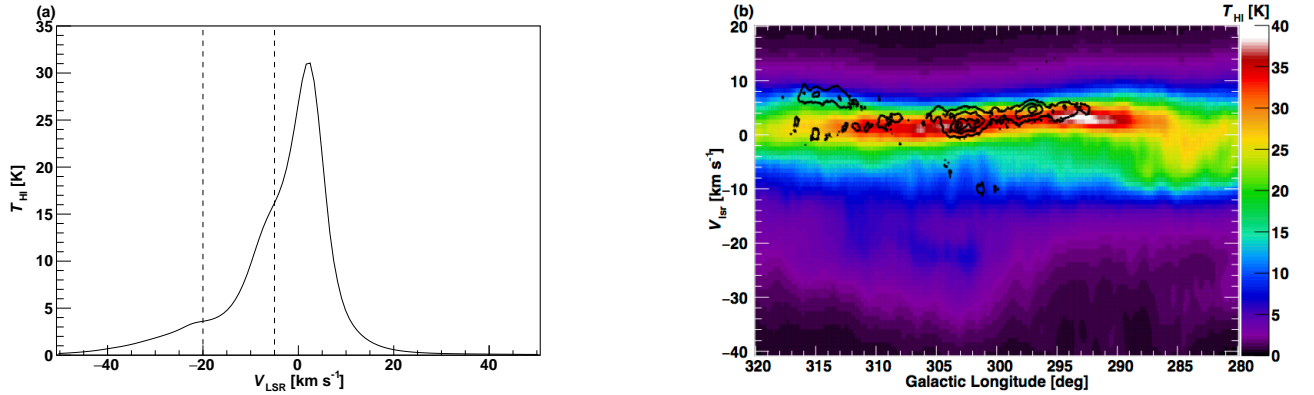


Figure 3. H I and $^{12}\text{CO } J=1-0$ velocity structures for the Chamaeleon region. (a) H I average spectrum giving the brightness temperature ($T_{\text{H I}}$) of the region analyzed. The vertical dashed lines indicate velocity boundaries roughly separated by eyes. Examples of the line profiles having the strong emission from the local, IVA and the high velocity components are shown in Figure 17. (b) Longitude-velocity diagram of the H I (image) and CO (contours) represented by the average intensities within the latitude range $-32^\circ \leq b \leq -12^\circ$. The CO contours are drawn every 0.25 K step from the minimum intensity 0.03 K ($\sim 3\sigma$).

3.4. Correlation between Gas and Dust Properties

We have investigated gas and dust properties using measurements of the *Planck* dust emission model and the near infrared extinction, A_J . The J -band wavelength ($\sim 1.25 \mu\text{m}$) is much larger than a typical size of the dust particle ($\lesssim 0.2 \mu\text{m}$; Jones et al. 2013) even if we take into account changing the size of a dust particle in its evolution (within $\sim 0.02 \mu\text{m}$; Ysard et al. 2015). Martin et al. (2012) suggests that the ratios of near-infrared color excess to N_{H} change less significantly in evolution process of the dust grains. These results expect that the ratio of A_J/N_{H} does not change significantly, indicating that A_J can be a tracer to measure the total gas column density.

Figure 4 shows a correlation plot between τ_{353} and A_J for the Chamaeleon region. Whereas most of the data are saturated in low A_J , data above a few 0.1 mag show a tight correlation with τ_{353} . The correlation between the two quantities above 0.32 mag ($\sim 4\sigma$ in A_J) is expressed by a regression line as follows,

$$\tau_{353} = [(1.35 \pm 0.05) \times 10^{-4}] \times A_J^{1.21 \pm 0.04}, \quad (1)$$

which is shown by the dashed line in the figure. This correlation between τ_{353} and A_J indicates that τ_{353} increases as equivalent to ~ 1.2 th power of N_H . Similar studies for the Orion A cloud (Roy et al. 2013) and the Perseus cloud (Okamoto et al. 2017) found that nonlinear relations between dust optical depth and N_H , whose power-law exponents are 1.28 ± 0.01 and 1.32 ± 0.04 , respectively. These authors make a point that the nonlinear relation is due to dust evolution effects. Although the correlation between gas and dust properties exhibits variations among the different regions, dust growth in the Chamaeleon region is also traced as the similar nonlinear relation with a power-law exponent of ~ 1.2 .

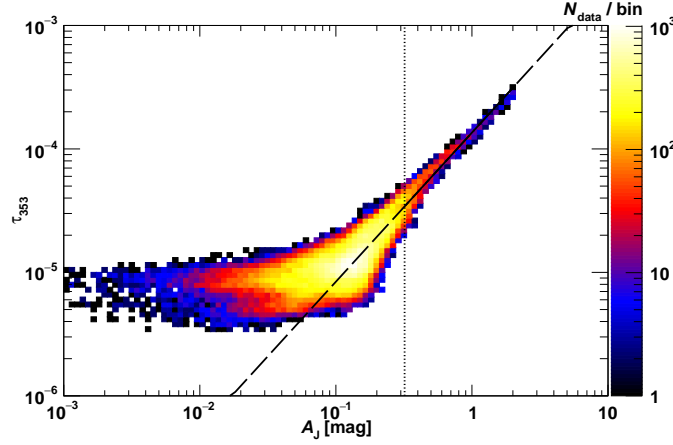


Figure 4. Correlation between A_J and τ_{353} . The dashed line indicates the best-fit linear regression, $\tau_{353} \propto A_J^{1.21 \pm 0.04}$ obtained by the fit to the data points above 0.32 mag ($\sim 4 \sigma$) in A_J shown by the vertical dotted line.

Figures 5(a) and (b) show correlation plots of τ_{353} with W_{H1} and W_{CO} , respectively, which are sorted by several T_d in 0.5 K intervals represented by different colors. To more clearly show the data points, the same density distribution plotted on different panels sorted by T_d are given in Figures 18 (τ_{353} – W_{H1}) and 19 (τ_{353} – W_{CO}). Although the correlation between τ_{353} and W_{H1} is poor overall, the data points sorted by T_d exhibit clearly different correlations depending on T_d : the scattering is small in high T_d areas and it becomes larger with decreasing T_d . The relationship with W_{CO} does not show a tight correlation either, even if we exclude noisy signals in W_{CO} below 1.2 K km s^{-1} ($\sim 3 \sigma$) and saturated ones above $\sim 8 \text{ K km s}^{-1}$. However, contrast in the dispersion among the different T_d is not large compared to the relation with W_{H1} . As shown in Figure 6, we have found an anti-correlation between τ_{353} and T_d probably related to feedback from the ISRF: in low density regions with lower τ_{353} , the ISRF heats up dust grains and leads to higher T_d . Conversely, in high density regions where τ_{353} is large, the ISRF is shielded by dust grains, which leads to lower T_d . Similar gas and dust properties are also found in other local molecular cloud complexes such as MBM 53–55 (F14) or Perseus (Okamoto et al. 2017) regions.

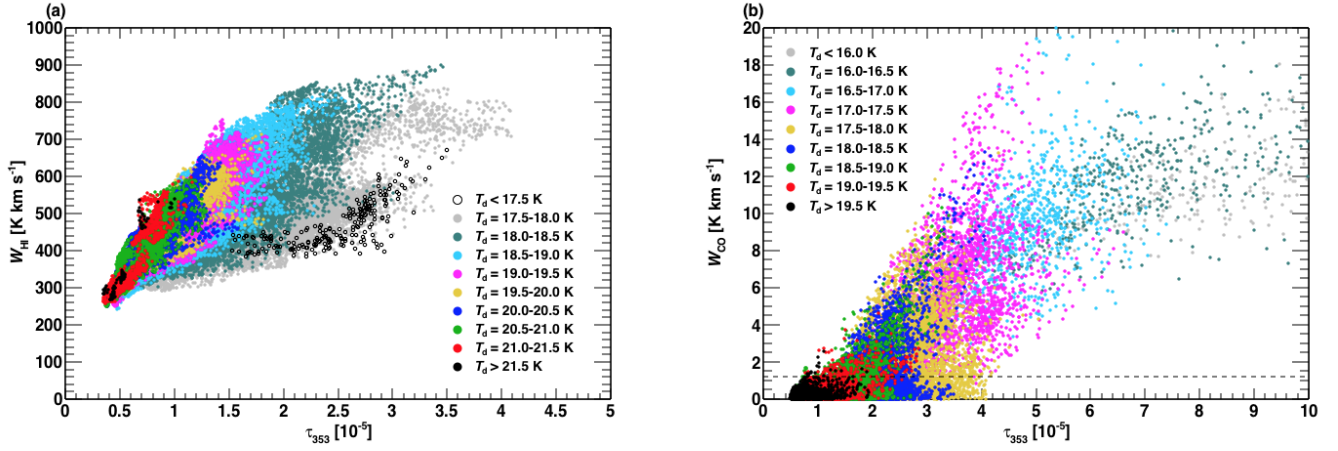


Figure 5. Correlation plots between (a) τ_{353} and W_{HI} and (b) τ_{353} and W_{CO} , sorted by several T_d intervals. The horizontal dashed line in the panel (b) indicates 3 σ confidence level in W_{CO} . The same plots shown in the different panels sorted by T_d are given in Figures 18 (τ_{353} – W_{HI}) and 19 (τ_{353} – W_{CO}).

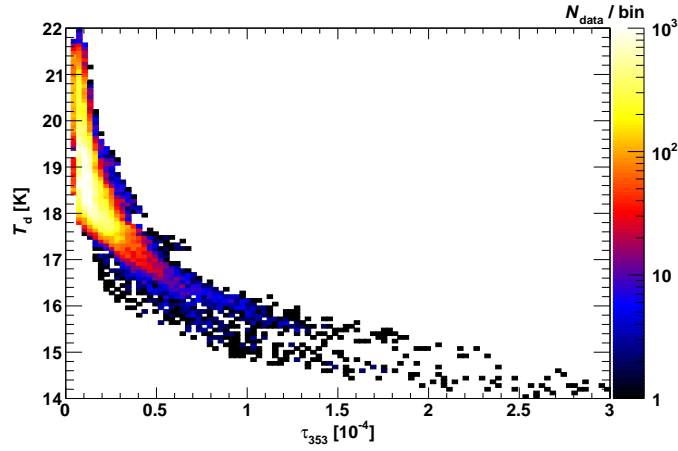


Figure 6. Correlation between τ_{353} and T_d .

4. MODELING THE GAS COLUMN DENSITY

The H I column density usually adopted as the optically thin limit (N_{HI}^*) is calculated from W_{HI} as follows,

$$N_{\text{HI}}^* = X_{\text{HI}} \times W_{\text{HI}}, \quad (2)$$

where $X_{\text{HI}} = 1.823 \times 10^{18} \text{ cm}^{-2} \text{ K}^{-1} \text{ km}^{-1} \text{ s}$. If the H I optical depth, τ_{HI} , does not satisfy $\tau_{\text{HI}} \ll 1$, this approximation underestimates the true H I column density. F14 and F15 adopted τ_{353} as an accurate tracer of N_{HI} and suggested possible large amount of the optically thick H I in the local ISM. F14 analyzed a molecular cloud region, MBM 53–55, whose gas density and star forming activities are relatively lower compared to other local molecular cloud regions (e.g., Yamamoto et al. 2003). The tight correlation between τ_{353} and W_{HI} in high T_{d} areas can be approximated well by a liner regression with small dispersion. The best-fit linear line is applied to the H I column density in the optically thin case (see Figure 3 in F14). Subsequently, F15 examined an N_{H} model with nonlinear relation with τ_{353} to consider dust evolution effect suggested by Roy et al. (2013). The model is expressed as,

$$\left(\frac{\tau_{353}}{\tau_{353,\text{ref}}} \right) = \left(\frac{N_{\text{H}}}{N_{\text{H,ref}}} \right)^\alpha \quad (3)$$

where $\tau_{353,\text{ref}}$ and $N_{\text{H,ref}}$ are reference points satisfying the relationship $N_{\text{H,ref}} = (1.15 \times 10^8) \times X_{\text{HI}} \times \tau_{353,\text{ref}}$ (Equation (2) in F15). Okamoto et al. (2017) applied the nonlinear N_{H} model to further investigate gas properties in Perseus molecular clouds and revealed that the N_{H} model with the ~ 1.3 th power more traces accurately the gaseous components from the diffuse medium to dense cores in the cloud complex.

Following the above studies, we have applied the nonlinear N_{H} model and examined a possibility of the optically thick H I in the Chamaeleon region. Based on an assumption of uniform gas-to-dust ratio in the local ISM, we have adopted the power-law index, $\alpha = 1.2$, which is derived from the τ_{353} – A_J relationship found in the opaque region (see Section 3.4). Although this gas-to-dust relation is not obtained from the diffuse H I medium, the similar nonlinearity is confirmed in Roy et al. (2013) down to $N_{\text{H}} \sim 1 \times 10^{21} \text{ cm}^{-2}$, which corresponds to the typical N_{H} discussed in F15 and Okamoto et al. (2017). If we take into account that the gas column density significantly affects the dust properties, this assumption is compatible as a first approximation to consider the dust evolution effect. The reference points in the N_{H} model are determined to be $\tau_{353,\text{ref}} = 7.8 \times 10^{-7}$ and $N_{\text{H,ref}} = 1.6 \times 10^{20} \text{ cm}^{-2}$, with an analytical method described in Appendix C. The N_{H} model is thus expressed as,

$$N_{\text{H}} = \left(\frac{\tau_{353}}{\tau_{353,\text{ref}}} \right)^{1/\alpha} \times N_{\text{H,ref}} = (2.0 \times 10^{25}) \times \tau_{353}^{1/1.2}. \quad (4)$$

Using the N_{H} model, we have modeled the scatter correlation between τ_{353} and W_{HI} with the following independent two equations (e.g., Dickey & Lockman 1990; Draine 2011): radiative transfer equation of the H I 21 cm line emission,

$$W_{\text{HI}} = (T_{\text{s}} - T_{\text{bg}}) \times \Delta V_{\text{HI}} \times \{1 - \exp(-\tau_{\text{HI}})\}, \quad (5)$$

and the H I optical depth derived from the H I spin flip transition,

$$\tau_{\text{HI}} = \frac{N_{\text{HI}}}{X_{\text{HI}}} \times \frac{1}{T_{\text{s}}} \times \frac{1}{\Delta V_{\text{HI}}}, \quad (6)$$

where ΔV_{HI} is spectral width in velocity, which can be defined as $W_{\text{HI}}/T_{\text{HI}}$.

Although T_{s} on the line of sight is not uniform, it can be approximated to a single component with a density-weighted harmonic mean in the line of sight (e.g., Dickey et al. 1979; Heiles & Troland 2003b; Fukui et al. 2018). By applying the N_{H} model in Equation (4) to the H I-dominated region (i.e., $N_{\text{H}} = N_{\text{HI}}$), a coupled equation between Equations (5) and (6) gives a theoretical model curve of W_{HI} as a function of τ_{353} ,

$$W_{\text{HI}} = \left(\left(\frac{\tau_{353}}{\tau_{353,\text{ref}}} \right)^{1/\alpha} \times \frac{N_{\text{H,ref}}}{X_{\text{HI}}} \times \frac{1}{\tau_{\text{HI}}} \times \frac{1}{\Delta V_{\text{HI}}} - T_{\text{bg}} \right) \times \Delta V_{\text{HI}} \times \{1 - \exp(-\tau_{\text{HI}})\}. \quad (7)$$

Applying average values in the analysis region, $\Delta V_{\text{HI}} = 13 \text{ km s}^{-1}$ and $T_{\text{bg}} = 3.7 \text{ K}$, which is estimated from the 21 cm radio continuum data, model curves with $\tau_{\text{HI}} \ll 1$, $\tau_{\text{HI}} = 0.34$, 1.0 and 2.0 are represented by the solid lines (from left to right) in Figure 7. For comparison, model curves with $\alpha = 1.0$ for the same τ_{HI} are also shown. The model curves with high τ_{HI} allows to reproduce the scatter correlation in high τ_{353} areas. The model with the nonlinear relation, $\alpha = 1.2$, traces better the mildly curved shape than $\alpha = 1.0$. This indicates that the N_{H} model in Equation (4) can approximately reproduce the gas distribution in the HI-dominated region. One can see a trend that τ_{HI} becomes larger with decreasing T_{d} , which indicates that there is a positive correlation between T_{d} and T_{s} . The contrast of the correlation strength among the different T_{d} in the τ_{353} – W_{CO} relationship (Figures 5(b) and 19) is not significant compared to the τ_{353} – W_{HI} relationship (Figures 5(a) and 18). The different correlation strength in the τ_{353} – W_{HI} relationship among T_{d} suggests existence of the atomic gas with low T_{s} (optically thick HI) around the molecular clouds.

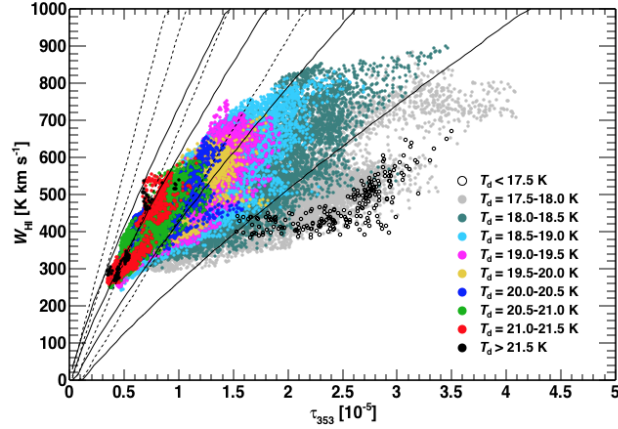


Figure 7. Correlation between τ_{353} and W_{HI} colored by T_{d} in 0.5 K windows. The solid and dotted curves show the theoretical functions of Equation (7) for $\alpha = 1.2$ and 1.0, respectively, with $\tau_{\text{HI}} \ll 1$, $\tau_{\text{HI}} = 0.34$, 1.0 and 2.0 from left to right. The same plots shown in different panels of each T_{d} are given in Figure 18.

5. DISCUSSION

5.1. Constituent of the Dark Gas

Our study of the Chamaeleon region showed that the optically thick H I is important around the molecular clouds. However, the previous γ -ray study (Planck Collaboration 2015) disagrees with the large amount of the optically thick H I. We discuss the cause of the contradiction below.

First, it is to be recognized that the γ -ray study assumes a uniform and a high H I spin temperature above 100 K, which is a strong assumption that pre-excludes the high H I optical depth. It is already shown by H I emission-absorption measurements (Heiles & Troland 2003b) that T_s , the harmonic mean T_s in a line of sight, is as low as 40 K and that low T_s is appreciable in the CNM. Further, T_s varies significantly from 30 K to more than 500 K, indicating that uniform high T_s is not supported. For realistic low T_s less than 100 K, H I optical depth is high, more than ~ 1.0 ; τ_{HI} derived from Equation (6) is ~ 1.1 at $N_{\text{HI}} = 1.0 \times 10^{21} \text{ cm}^{-2}$, close to the peak of N_{HI} distribution, and $\Delta V_{\text{HI}} = 5 \text{ km s}^{-1}$, a typical line width of the CNM (c.f., F15). We note if τ_{HI} is greater than 0.3 and 0.5, the optical depth correction by a factor of 1.2 and 1.3, respectively, is required in calculating N_{H} . In this sense, the boundary between optically thick or thin H I lines at τ_{HI} of 0.3–0.5, depending on the accuracy needed, and the optically thin case is for τ_{HI} less than 0.2 in the practical H I sensitivity. We expect that optically thick H I is suggested by a γ -ray study if the unrealistic assumption of the uniform high T_s is not adopted.

It is discussed in the literature both observational and theoretical that there exists a significant amount of CO-dark H_2 gas (e.g., Wolfire et al. 2010; Liszt et al. 2018). We discuss critically these works below, and look into the cause of the apparent discrepancy.

- Observations of molecular abundance are often used to estimate molecular fraction in the low density molecular gas. Since absorption measurements toward radio continuum sources like quasars are more sensitive than emission line measurements, compact continuum sources are used to measure molecular absorption of HCO^+ , HCN etc (e.g., Liszt & Gerin 2016; Liszt et al. 2018; Gerin et al. 2019). Detection of such molecular absorption shows that such rare molecules do exist in the low density gas where the gas may not be detectable in CO emission due to low density. Liszt et al. (2018) assumed that abundance ratio between HCO^+ and H_2 is uniform at 3×10^{-9} to derive H_2 density and argued that CO-dark H_2 gas may contribute significantly as the dark gas. These authors derived high CO intensity by assuming the $X_{\text{CO}} = 2 \times 10^{20} \text{ cm}^{-2} \text{ K}^{-1} \text{ km}^{-1} \text{ s}$, which is about 2 times higher than those obtained by recent studies of the Chamaeleon region (Ackermann et al. 2012; Planck Collaboration 2015), and showed that the predicted CO intensity disagrees with the non-detection of CO by NANTEN by a factor of more than 2 at several points in these clouds. It is probable that their method is not accurate in the order of 10%, because the molecular abundance varies significantly from place to place; Gerin et al. (2019) showed that HCO^+ abundance by ALMA observations, for instance, varies by an order of magnitude for density around N_{H} of 10^{20} cm^{-2} (see their figure 4), and the assumption of uniform HCO^+ abundance by Liszt et al. (2018) is not supported. The large discrepancy above in the expected CO intensity is explained as due to the unrealistic assumption of uniform HCO^+ abundance. In summary, the HCO^+ absorption is not an accurate method to calculate H_2 abundance because of the small and variable abundance, and the mass estimate of CO-dark gas is uncertainty by a factor of 2–3 at best. Accordingly, the molecular absorption is not accurate enough to constrain the dark molecular gas.
- Wolfire et al. (2010) made a theoretical study of CO-dark H_2 by using calculations of molecular abundance in a model cloud, and concluded that CO-dark gas is significant. This study assumes as the initial condition that the gas density is as high as 10^3 cm^{-3} , where hydrogen exists mostly as H_2 . It is a question if the initial condition is justified. Inoue & Inutsuka (2012) showed how molecular gas is formed in the interstellar space by taking H I gas as the initial condition. This is a more general assumption and their results show that H I gas remains significant even after the convergence of H I flows after 10 Myrs. The results suggest a mixture of H I and H_2 gas as the state of the realistic interstellar molecular gas. Therefore, the fraction of H_2 is highly dependent on the initial condition. Since molecular gas is formed from atomic gas, any simulations assuming pure H_2 as the initial condition needs justification before confronting with observations.

Fukui et al. (2018) performed a synthetic observation of the interstellar gas based on the results of Inoue & Inutsuka (2012). They applied molecular fraction measured by UV absorption (Gillmon et al. 2006) to that of the simulated interstellar gas, whose N_{H} is peaked at $\sim 1 \times 10^{21} \text{ cm}^{-2}$ in a range from $5 \times 10^{20} \text{ cm}^{-2}$ to $2 \times 10^{21} \text{ cm}^{-2}$, which is

consistent with the N_{H} distribution obtained by the τ_{353} -based N_{H} model (see figure 4 in Fukui et al. 2018). The results showed that the CNM has clumpy gas distribution with volume filling factor ($\sim 4\%$) and gas density ($10^2\text{--}10^3\text{ cm}^{-2}$), which are consistent with generally suggested gas properties of the ISM; the gas masses of the CNM and WNM are comparable, while their density fraction is estimated to be 30:1 and thus the ratio of the volume filling factor is 1:30 (e.g., Dopita & Sutherland 2003). The fraction of the CNM in $\int \tau_{\text{H I}} dv$ does not contradict the H I emission-absorption measurements by Heiles & Troland (2003a) (see Figure 13 in Fukui et al. 2018). The simulation showed that the fraction of H_2 is only $\sim 5\%$.

From the above discussions, we conclude that in the Chamaeleon region optically thick H I is more important than CO-dark H_2 and thus a dominant constituent of the dark gas. Hereafter we discuss gas properties and distribution, focusing on the optically thick H I.

5.2. Gas Distribution and Mass Fraction

With the N_{H} model in Equation (4), we discuss H I gas properties and mass fractions in the cloud complex. We have solved the coupled equations between Equations (5) and (6) and derived $\tau_{\text{H I}}$ and T_{s} values by numerical solution. Figures 8(a)–(d) show examples of the solution for the corresponding positions. The blue and red lines indicate Equations (5) and (6), respectively, and the obtained $\tau_{\text{H I}}$ and T_{s} are shown by the purple solid line. The dashed lines indicate 1σ error limits. The errors in the obtained $\tau_{\text{H I}}$ and T_{s} are given by the dashed crossing points. These examples give solutions ($\tau_{\text{H I}}, T_{\text{s}}$ (K)) $\sim (1.9, 40), (1.2, 60), (0.6, 80), \text{ and } (0.3, 100)$.

Figures 9(a) and (b) respectively show distributions of $N_{\text{H I}}$ generated with the $\tau_{\text{H I}}$ and T_{s} values and N_{H} expressed by Equation (4). In the $N_{\text{H I}}$ map, the CO-dominated region is masked. The high column H I around the molecular clouds ($N_{\text{H I}} \gtrsim 2 \times 10^{21}\text{ cm}^{-2}$) indicates a large amount and extent of the optically thick H I. Its distribution is similar to those of high τ_{353} ($\gtrsim 1 \times 10^{-5}$) and low T_{d} ($\lesssim 18\text{ K}$) (see Figure 1). Physical association between the H I gas and dust properties are confirmed in the spatial distribution.

Figures 10(a), (b) and (c) show mass-weighted histograms of $\tau_{\text{H I}}$, T_{s} and $N_{\text{H I}}$ in the analysis region, respectively. The obtained N_{H} histogram is also plotted in the panel (c). For the mass calculation, we have assumed the distance for the Chamaeleon region 150 pc and adopted the mean atomic mass per H atom, $\mu = 1.41$ (Däppen 2000). Average values for $\tau_{\text{H I}}$ and T_{s} are ~ 1.3 and $\sim 63\text{ K}$, respectively, which suggests large optical depth in the H I-dominated region. The $N_{\text{H I}}$ spans $\sim (0.5\text{--}4) \times 10^{21}\text{ cm}^{-2}$ with the average value of $\sim 1.8 \times 10^{21}\text{ cm}^{-2}$. The typical H_2 column density estimated from subtraction of $N_{\text{H I}}$ from N_{H} is $\sim 1.5 \times 10^{21}\text{ cm}^{-2}$, which is consistent with that obtained by the numerical simulation (Figure 4 in Fukui et al. 2018). Gas masses of the atomic hydrogen excluding the CO-emitting region and the total hydrogen including the molecular gas are $\sim 6.3 \times 10^4 M_{\odot}$ and $\sim 8.3 \times 10^4 M_{\odot}$, respectively. Our result indicates that the total mass is $\sim 30\%$ larger than the estimates in Planck Collaboration (2015). The subtraction of the mass of the atomic gas component from the total mass, $\sim 2.0 \times 10^4 M_{\odot}$, is much larger than the molecular gas mass $\sim 5000\text{--}8000 M_{\odot}$ estimated by previous studies (e.g., Mizuno et al. 2001; Ackermann et al. 2012; Planck Collaboration 2015). This can be understood by the H I gas probably distributed in front and behind the molecular clouds.

Planck Collaboration (2015) and Remy et al. (2018) pointed that the large gas column density inferred from the optically thick H I scenario should lower the local γ -ray emissivity, and thus yield a cosmic-ray density different from results of direct cosmic-ray measurements. However, our τ_{353} -based N_{H} model with the nonlinear effect lowered the column density compared to the linear relation with τ_{353} (F14; F15) and derived the total gas mass different from Planck Collaboration (2015) by $\sim 30\%$, which is within uncertainty of the measurements of the local γ -ray emissivity (see Table E.1 in Planck Collaboration 2015). This result indicates that our τ_{353} -based N_{H} model is acceptable in terms of the γ -ray studies.

Here we discuss an insight of the CO-dark H_2 in case of our τ_{353} -based N_{H} model. If we assume that all the H I emission is optically thin, the mass of the atomic gas for the Chamaeleon region is derived to be $\sim 4.1 \times 10^4 M_{\odot}$. Given that the CO-dark H_2 contributes to 50% of the dark gas, the molecular gas mass for our derived total gas mass is estimated to be $\sim 25\%$ ($\sim 2 \times 10^4 M_{\odot}$), which is 3–4 times larger than the gas mass traced by CO. This fraction is much larger than those estimated in other observational studies (Planck Collaboration 2015) and theoretical predictions (e.g., Levrier et al. 2012), where the CO-dark H_2 is a dominant component of the dark gas. Although the CO-dark H_2 increases the total gas budget as suggested by many studies of molecular line surveys, we have not found evidence for the large mass of molecular gas as the dark-gas component.

Our results support the optically thick H I scenario, but we found a contradiction with previous studies of the local H I gas properties. Stanimirović et al. (2014) derived that a CNM fraction for Perseus molecular cloud is $\lesssim 0.5$ at the dark-gas medium where $N_{\text{HI}} \gtrsim 1 \times 10^{20} \text{ cm}^{-2}$ (see Figure 8 in that paper). This CNM fraction is almost consistent with Fukui et al. (2018). Meanwhile, our N_{H} model shows $\tau_{\text{HI}} \gtrsim 1$ at the dark-gas medium and thus suggests that the CNM is dominant there, which is not consistent with the slightly lower CNM fractions estimated by Stanimirović et al. (2014) and Fukui et al. (2018). The cause of this discrepancy is not clear. To reveal the difference among these studies, further evaluations of our gas model (e.g., variations of τ_{HI} and T_{s} due to uncertainty of the N_{H} model and ΔV_{HI}) are required, as well as a number of H I emission-absorption measurements for the dark-gas medium of the Chamaeleon region.

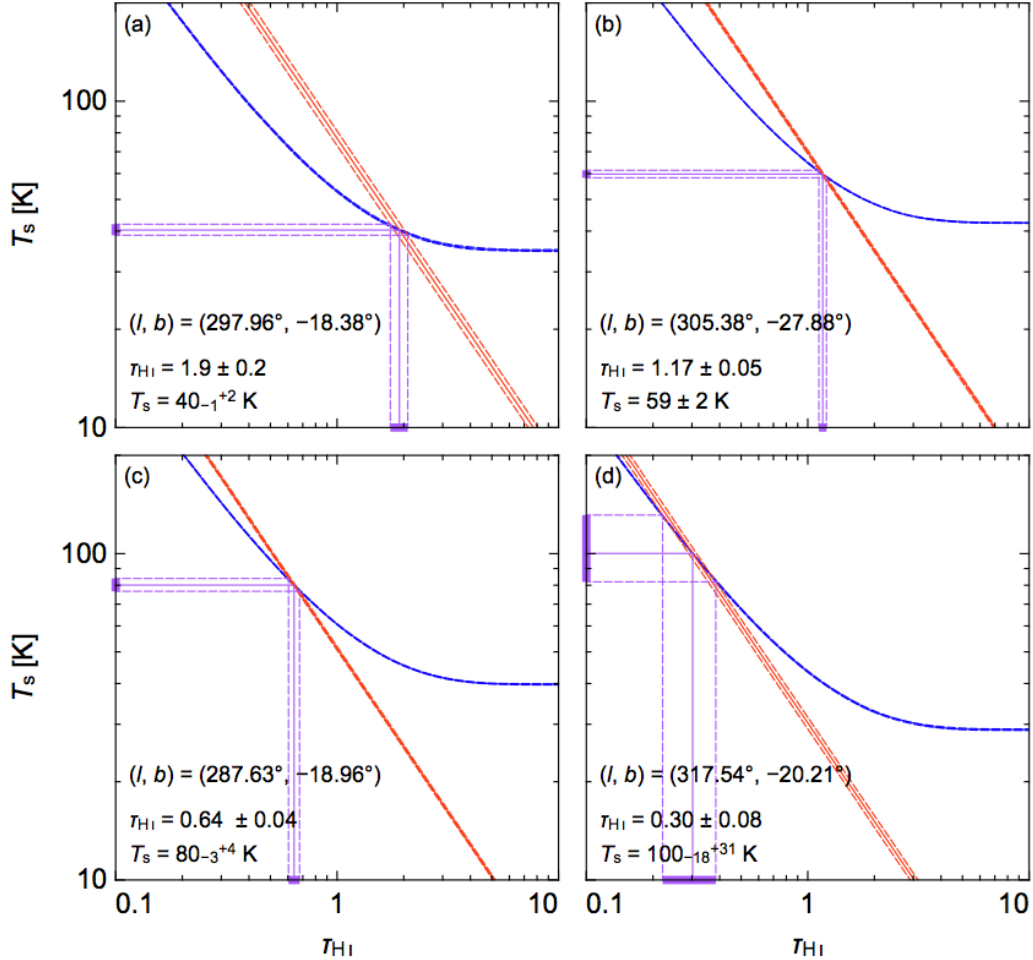


Figure 8. Examples of the τ_{HI} and T_{s} calculations. The blue and red solid lines indicate Equations (5) and (6), respectively. The purple solid lines show the solution of τ_{HI} and T_{s} . The dashed lines of each color indicate 1σ error limit.

5.3. X_{CO} Distribution

The CO-to-H₂ conversion factor, X_{CO} , is usually estimated as $\sim(1-2) \times 10^{20} \text{ cm}^{-2} \text{ K}^{-1} \text{ km}^{-1} \text{ s}$ in the Milky Way disk (e.g., Bolatto et al. 2013). Using our τ_{353} -based N_{H} model, we can calculate X_{CO} from a correlation with W_{CO} as described below. The total column density N_{H} is expressed as a sum of the number of protons in N_{HI} and N_{H_2} ,

$$N_{\text{H}} = N_{\text{HI}} + 2N_{\text{H}_2}. \quad (8)$$

By substituting $X_{\text{CO}} (\equiv N_{\text{H}_2}/W_{\text{CO}})$ into Equation (8), the correlation between W_{CO} and N_{H} is expressed as,

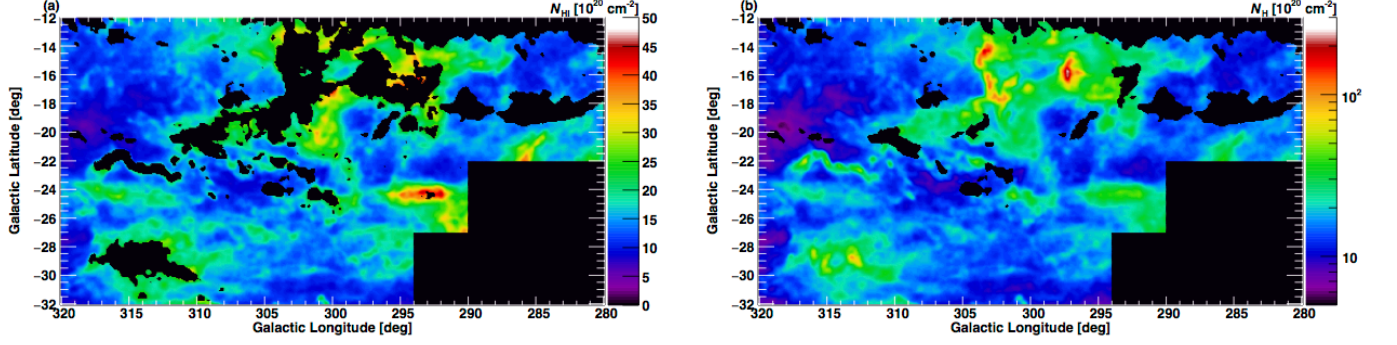


Figure 9. (a) Atomic (N_{HI}) and (b) total hydrogen (N_{H}) column density maps. The CO-emitting region is masked in the N_{HI} map.

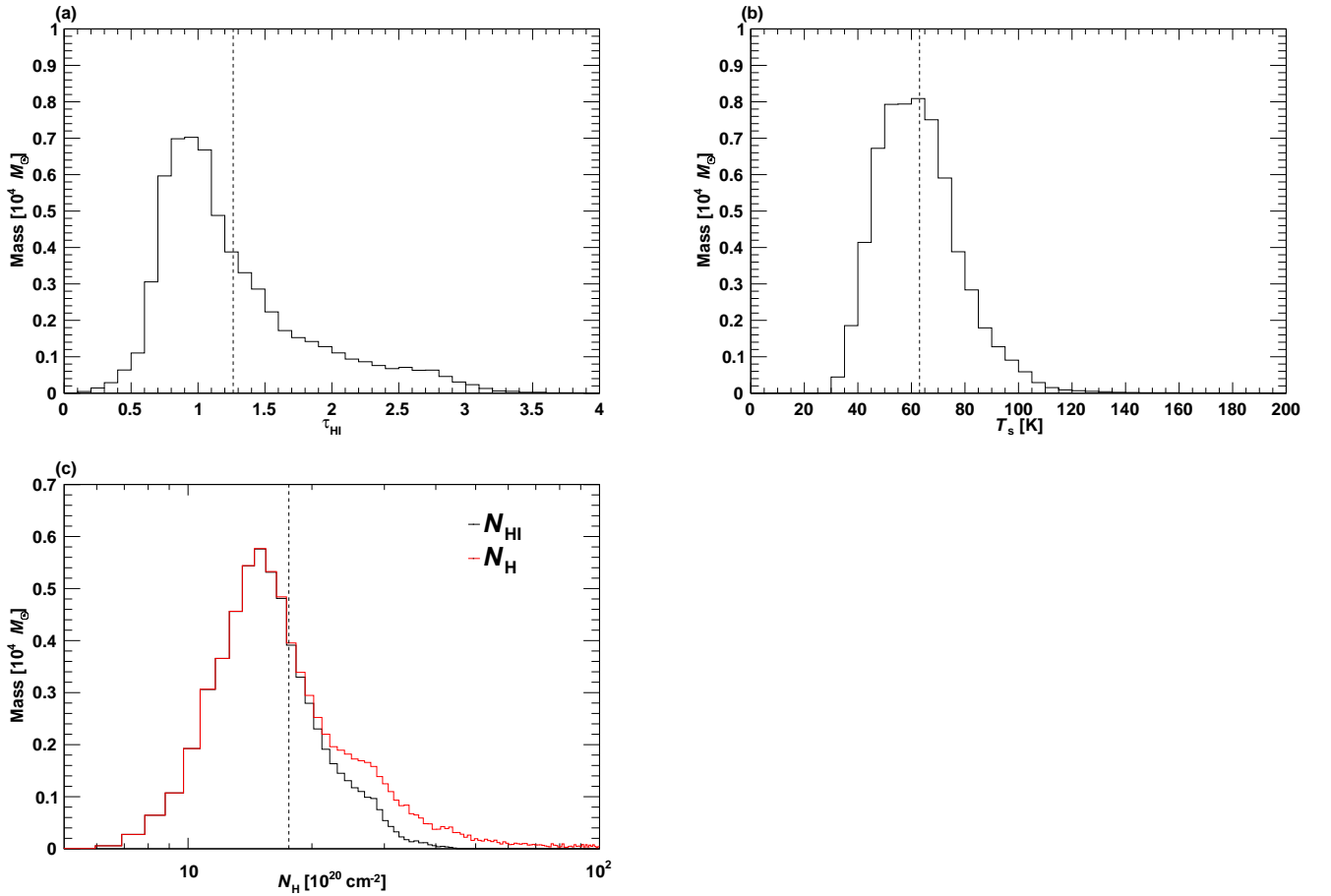


Figure 10. Mass-weighted histograms of (a) τ_{HI} , (b) T_s and (c) N_{HI} (black) and N_{H} (red). The vertical dashed lines indicate the mass-weighted mean values, $\langle \tau_{\text{HI}} \rangle = 1.3$, $\langle T_s \rangle = 63$ K and $\langle N_{\text{HI}} \rangle = 1.8 \times 10^{21} \text{ cm}^{-2}$.

$$N_{\text{H}} = (2X_{\text{CO}}) \times W_{\text{CO}} + N_{\text{HI}} = (\text{slope}) \times W_{\text{CO}} + (\text{intercept}). \quad (9)$$

The half value of the slope gives an X_{CO} factor.

Figure 11 shows a relationship between W_{CO} and N_{H} for the entire analysis region. One can see a positive correlation especially at low W_{CO} . However, significant deviation is seen at $W_{\text{CO}} \gtrsim 8 \text{ K km s}^{-1}$, probably due to saturation of

the optically thick $^{12}\text{CO } J=1-0$ line often found in CO cores. In Figures 12 (a)–(c), we make the same scatter plots whose data points are taken from the major clouds of the Chamaeleon region, Cha I, II and III, which are covered by areas (a)–(c) as shown in Figure 13. The significant deviation is found at high W_{CO} especially in areas (a) and (c), which yield the large scattering in the $W_{\text{CO}}-N_{\text{H}}$ relationship in Figure 11.

Recent studies of the ISM suggest that the X_{CO} have variations in a cloud complex depending on surrounding interstellar environment (e.g., Bell et al. 2006; Lee et al. 2014; Okamoto et al. 2017). To derive a spatial distribution of X_{CO} from the $W_{\text{CO}}-N_{\text{H}}$ relationship, we divided the analysis region into $1.5^\circ \times 1.5^\circ$ regions, and fit the data points with a linear function for each region that has the number of data points above 30 and the correlation coefficient above 0.7. At first, the fitting range in W_{CO} is restricted to from 1.2 K km s^{-1} to 5 K km s^{-1} , to exclude contamination in W_{CO} lower than the detection limit and the saturation effect at high W_{CO} . Then we gradually raised the upper limit of the fitting range every 0.5 K km s^{-1} . The values of X_{CO} derived with $W_{\text{CO}} < 7.5 \text{ K km s}^{-1}$ are consistent with those of $< 5 \text{ K km s}^{-1}$ within the statistical errors except for the regions where the data points at high W_{CO} ($\gtrsim 8 \text{ K km s}^{-1}$) dominate. We therefore adopted the X_{CO} obtained from the fitting range at $1.2 \text{ K km s}^{-1} < W_{\text{CO}} < 7.5 \text{ K km s}^{-1}$. The derived $1.5^\circ \times 1.5^\circ$ -based X_{CO} map is shown in the panel (a) of Figure 21, having some blanks in the diffuse medium where the value of X_{CO} cannot be determined due to low statistics of the data and/or poor correlation of the $W_{\text{CO}}-N_{\text{H}}$ relationship. To compensate the low data statistics, we extended the size of the fitting area to $2^\circ \times 2^\circ$ and $2.5^\circ \times 2.5^\circ$ regions, whose results are shown in the panels (b) and (c) of Figure 21, respectively. In these maps, X_{CO} for the blank regions found in the $1.5^\circ \times 1.5^\circ$ -based map is given owing to increase of the data points. On the other hand, the larger pixelized map possibly overlooks local variation of X_{CO} such as a region at $(l, b) \sim (304^\circ, -14.5^\circ)$, where the X_{CO} values of the $1.5^\circ \times 1.5^\circ$ -based map are significantly different from the other two maps. We therefore combined the three X_{CO} maps, preferentially adopting the X_{CO} from the $1.5^\circ \times 1.5^\circ$ -based map; the other two maps are used to compensate the blank regions. The finally obtained X_{CO} map is shown in Figure 13. The X_{CO} spans $\sim (0.5-3) \times 10^{20} \text{ cm}^{-2} \text{ K}^{-1} \text{ km}^{-1} \text{ s}$ across the cloud complex and the average one derived from Figure 11 is $1.4 \pm 0.1 \times 10^{20} \text{ cm}^{-2} \text{ K}^{-1} \text{ km}^{-1} \text{ s}$. These values are consistent with the typical X_{CO} measured for the Galactic interstellar clouds, $(1-2) \times 10^{20} \text{ cm}^{-2} \text{ K}^{-1} \text{ km}^{-1} \text{ s}$ (e.g., Bolatto et al. 2013). A study of the ISM of the Chamaeleon region, Planck Collaboration (2015), also derives an X_{CO} factor comparable to our result through their analysis using the dust optical depth, τ_{353} .

In Figures 12 (d)–(h), we show the correlation plot for the regions enclosed by the dashed lines in the X_{CO} map in Figure 13. These regions are selected to more clearly show and discuss possible relations between the X_{CO} and the surrounding gas condition. We fit the data points with a linear function similarly to Figure 11 and found that each region shows a good correlation, but their slopes vary depending on their positions. In addition to the X_{CO} , the fitting also gives the intercept values of N_{H} , as represented by the red-dashed lines in Figure 12 (also in Figure 11 as an average value for the entire analysis region). These values correspond to average H I column density in each fitted region and are comparable to the N_{H} around the masked CO-dominated region shown in Figure 9(a).

The Chamaeleon complex consists of Cha I–III, Cha-East I, Cha-East II, and Major Filament, having different evolutionary history and star formation activity (Mizuno et al. 2001). We found X_{CO} at $303^\circ \lesssim l \lesssim 304^\circ$ in Cha II and Cha III, and the whole cloud of Cha I show relatively high values, $\sim (1.5-3) \times 10^{20} \text{ cm}^{-2} \text{ K}^{-1} \text{ km}^{-1} \text{ s}$, as shown by the correlations for areas (d) and (f). Cha-East I including area (g) also has a relatively high X_{CO} ($\sim 1.5 \times 10^{20} \text{ cm}^{-2} \text{ K}^{-1} \text{ km}^{-1} \text{ s}$). Conversely, X_{CO} at $300^\circ \lesssim l \lesssim 301^\circ$ in Cha II, where a part of area (e) is included, is relatively small ($\lesssim 1 \times 10^{20} \text{ cm}^{-2} \text{ K}^{-1} \text{ km}^{-1} \text{ s}$). Cha-East II and Major Filament also show similar low X_{CO} . The N_{H} map in Figure 9(a) indicates that areas (d) and (g) are faced to the interstellar space with relatively low column density ($\sim 1.5 \times 10^{21} \text{ cm}^{-2}$), while the N_{H} surrounding area (e) and Major Filament is rather high ($\sim 2-3.5 \times 10^{21} \text{ cm}^{-2}$). The large X_{CO} in areas (d) and (g) is probably due to CO destruction in the low-density medium, while the small X_{CO} in area (e) could be ascribed by sufficient dust shielding with the visual extinction, $A_v \gtrsim 1 \text{ mag}$ ($A_J \gtrsim 0.3 \text{ mag}$), preventing CO from photodissociation. The trend of high X_{CO} in regions with low CO abundance outside molecular clouds is consistent with observational studies of molecular cloud regions (e.g., Cotten & Magnani 2013; Okamoto et al. 2017) and theoretical predictions of formation of molecular clouds (e.g., Inoue & Inutsuka (2012)).

Among the six cloudlets in the Chamaeleon complex, Cha I exhibits the highest star formation activity represented by two Ae/Be stars located in the CO core (Luhman 2008). The relatively high X_{CO} around the CO cores in Cha I, exemplified by area (f) ($X_{\text{CO}} \sim 1.7 \times 10^{20} \text{ cm}^{-2} \text{ K}^{-1} \text{ km}^{-1} \text{ s}$), may be ascribed to the more intense radiation field and enhanced stellar feedback, suggesting preferential destruction of CO in the star-forming region. Cha II holds a few tens of young stellar objects at $303^\circ \lesssim l \lesssim 304^\circ$ and $-15^\circ \lesssim b \lesssim -13.5^\circ$ (Alcalá et al. 2008), which nearly corresponds

to the positions with the highest $X_{\text{CO}} \sim 3.0 \times 10^{20} \text{ cm}^{-2} \text{ K}^{-1} \text{ km}^{-1} \text{ s}$, possibly showing the gas properties related to an evolutionary step of the low-mass stars. On the other hand, Cha-East II has relatively lower X_{CO} as seen in the correlation for area (h). This result makes sense in terms of no strong radiation field in the surrounding medium and lack of star-forming activity in the CO cores of the clouds.

Finally, we note a peculiar correlation found in the CO core of Cha II. We found that the $W_{\text{CO}}-N_{\text{H}}$ relationship in area (e) shows a tight correlation without the W_{CO} saturation, in spite of inclusion of the data points at high W_{CO} ($\gtrsim 10 \text{ K km s}^{-1}$). This trend is also confirmed in the $\tau_{353}-W_{\text{CO}}$ relationship of Figures 5(b) and 19, as a scatter distribution at $\tau_{353} \sim 4 \times 10^{-5}$ and $W_{\text{CO}} > 10 \text{ K km s}^{-1}$. One of the possibility of the high value of W_{CO} is due to a high CO abundance in this region, suggesting possible different age of the molecular gas and a different evolutionary history of the clouds in the Chamaeleon region. The other possibility of the lower saturation is opacity effect of the CO line. Figure 14 shows CO spectra for the Cha I-III regions, whose intensities are summed for the pixels in areas (a)–(c). We confirmed that the spectrum of the Cha II (area (a)) is more broaden than those of the others, which may suggest gas turbulence leading to lower the opacity of the cloud. A few tens of young stellar objects are included in the Cha II region (Alcalá et al. 2008) and thus possible outflows may contribute this effect, as similarly suggested in a star-forming region of the Perseus molecular cloud (Pineda et al. 2008).

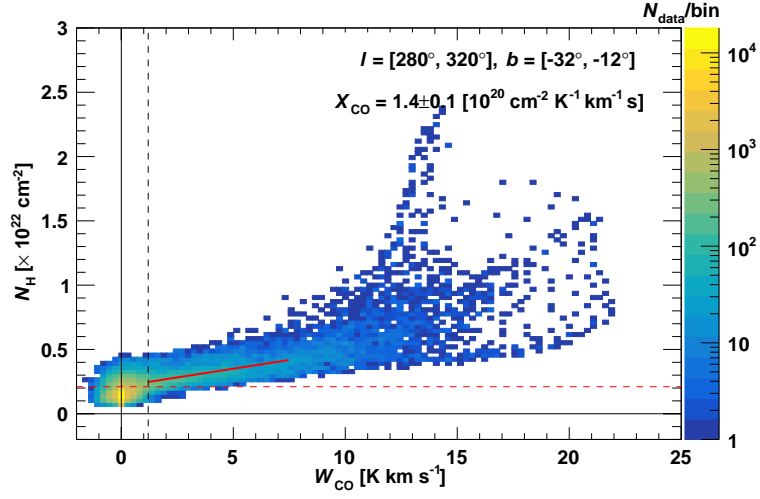


Figure 11. $W_{\text{CO}}-N_{\text{H}}$ correlation plots for the all data points in the analysis region. The red solid line indicates the best-fit regression line obtained by the fit to the data points at $1.2 \text{ K km s}^{-1} (3 \sigma) < W_{\text{CO}} < 7.5 \text{ K km s}^{-1}$. The vertical dashed line shows the lower limit of the fitting range. The horizontal red dashed line indicates the intercept value of N_{H} obtained by the fitting.

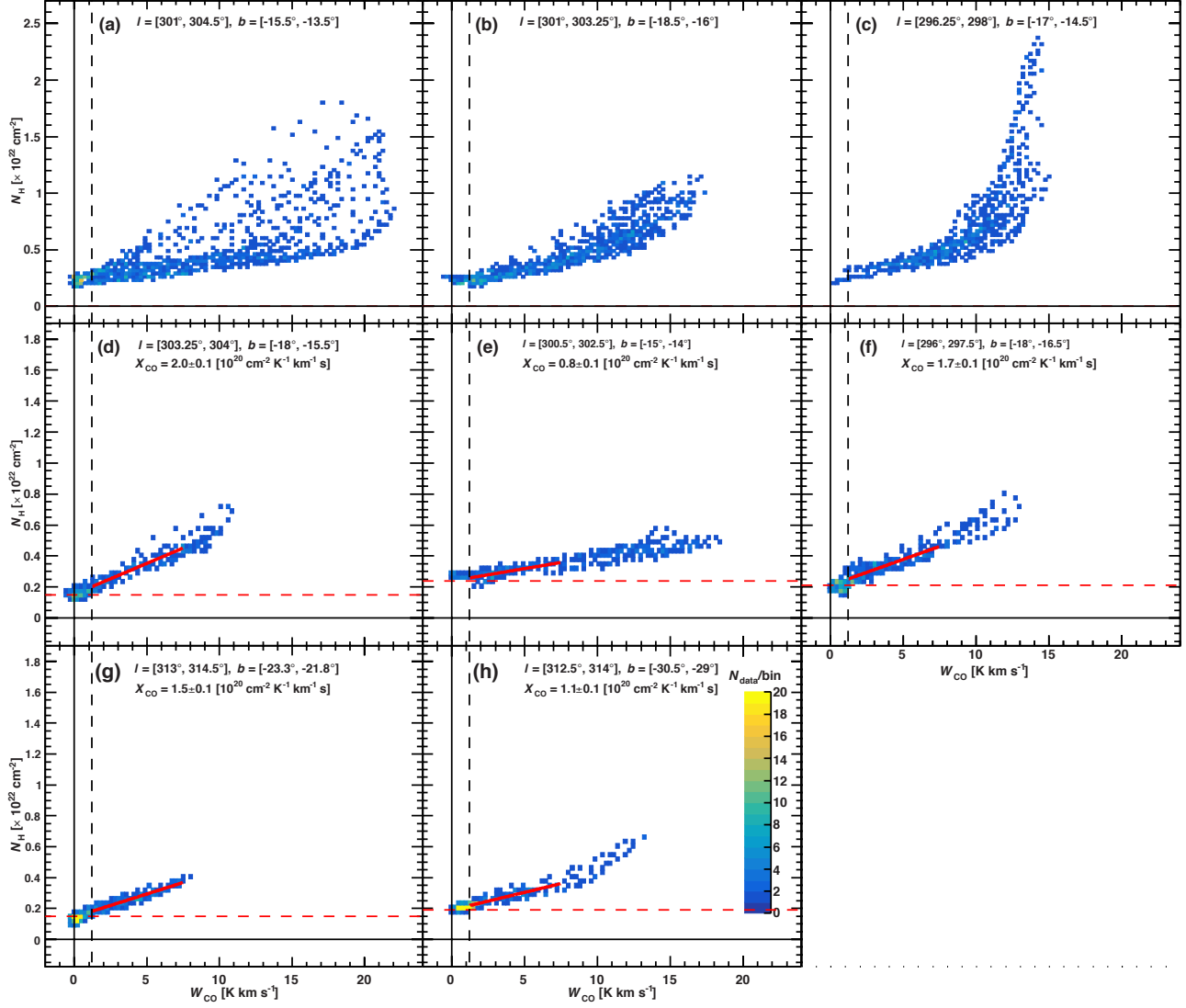


Figure 12. $W_{\text{CO}}-N_{\text{H}}$ correlation plots with the data points taken from the areas (a)–(h) in Figure 13. The meaning of the lines in each panel are the same as Figure 11.

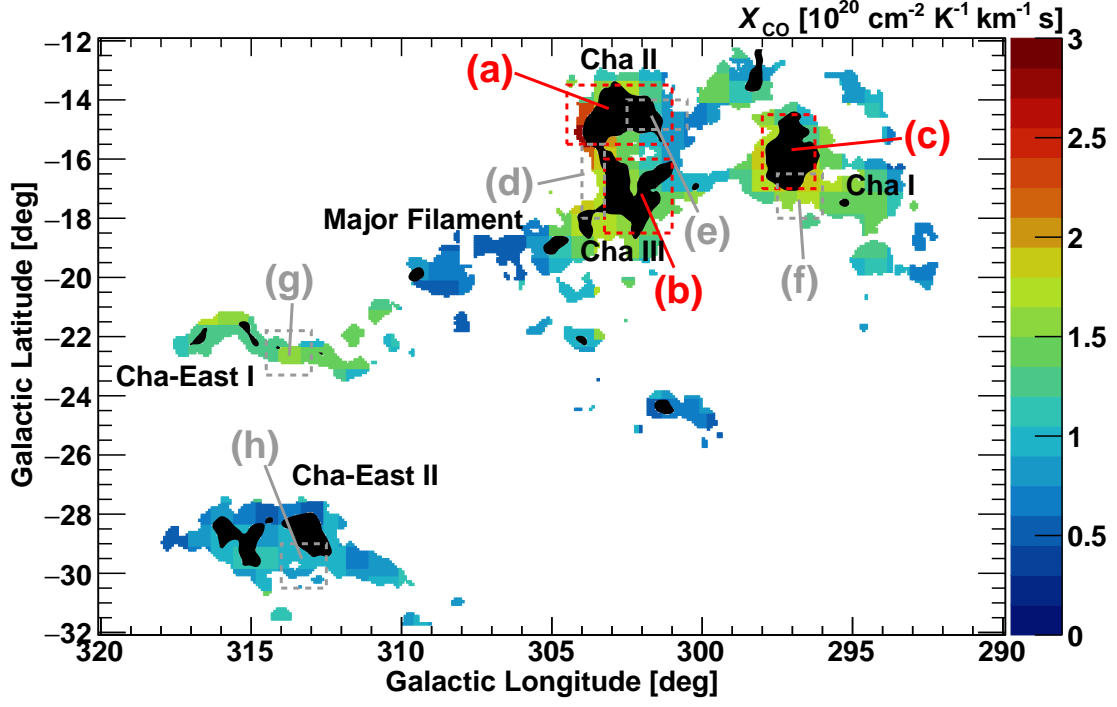


Figure 13. X_{CO} distribution derived from the correlation between W_{CO} and N_{H} . The areas (a)–(h) correspond to the correlation plots in Figures 12(a)–(h), respectively. The black-filled areas indicate regions with $W_{\text{CO}} > 7.5 \text{ K km s}^{-1}$. The deriving method of the map is described in the text of Section 5.3 and Figure 21.

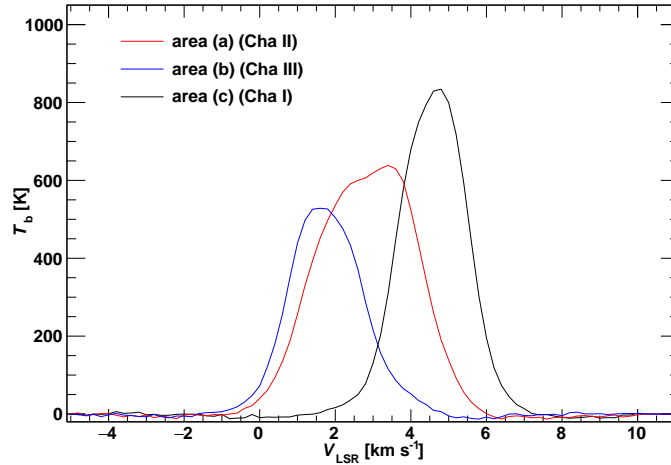


Figure 14. The spectra of $^{12}\text{CO } J=1-0$ for areas (a), (b) and (c) shown in Figure 13. The brightness temperature (T_b) on the y-axis is a sum of T_b of each pixel of the W_{CO} map in Figure 1 (a).

5.4. Comparison with Other Molecular Cloud Regions

Finally, we compare gas properties among local molecular cloud complexes, MBM 53–55 (F14), Perseus (Okamoto et al. 2017), and Chamaeleon (this study) regions, for which dedicated analyses have been performed with our τ_{353} -based N_{H} model. The τ_{353} – W_{HI} correlation plots of each region are shown in Figures 15(a)–(c). For easier comparison, the horizontal and vertical ranges in the panel (a) are shown in the panels (b) and (c). Table 1 summarizes physical quantities obtained by these studies.

τ_{353} in MBM 53–55 region is approximately one order of magnitude smaller than those in the other two regions, which yields relatively lower N_{H} . The large τ_{353} in the Perseus and Chamaeleon regions gives larger N_{H} , although it is unlikely to increase with a simple linear function of τ_{353} . We have found a nonlinear relation with $\alpha \sim 1.2$ – 1.3 in the τ_{353} – A_J relationship for the dense molecular clouds ($A_J \gtrsim 0.3$ mag) of the Perseus and Chamaeleon regions. This nonlinear relation also traces the mild curvature in the τ_{353} – W_{HI} relationship for the H I-dominated medium, which is clearly different from the linear relation seen in the MBM 53–55 region (see Figure 15). These variations of dust opacity may arise from different grain evolution among the cloud complexes. Taking into account the dust evolution effect, the N_{H} for the Perseus and Chamaeleon regions are found to be larger by factor of ~ 2 – 6 than that for the MBM 53–55 region.

The total column density model as a function of τ_{353} allows us to investigate the atomic and molecular gas properties. The obtained $\langle T_{\text{s}} \rangle$ is the highest in Perseus region and it becomes lower followed by Chamaeleon and MBM 53–55 regions. The trend of dust evolution (α) and the H I gas properties (T_{s} and τ_{HI}) might be associated with current star-forming activities: less star formation in the MBM 53–55 clouds (e.g., Yamamoto et al. 2003), high-mass star-formation in the Perseus (e.g., Bally et al. 2008) and low-mass star-formation in the Chamaeleon (e.g., Luhman 2008) regions. The Perseus molecular clouds are included in the Perseus OB2 Association, which forms a part of Golds Belt. Massive stars located in this region may heat the surroundings atomic gas and generate relatively higher T_{s} . The MBM 53–55 region shows the largest $\langle \tau_{\text{HI}} \rangle$, which indicates a large amount of dark gas between the H I and CO transition. This is consistent with the large mass fraction of dark gas in this region suggested by a γ -ray analysis (Mizuno et al. 2016). The relatively lower α suggests less dust evolution, which may relate to the lower current star-formation activity. The X_{CO} becomes smaller in the MBM 53–55 region and larger in the Perseus region. According to recent studies of X_{CO} in the local interstellar clouds, X_{CO} in high-density regions tends to be lower (e.g., Cotten & Magnani 2013; Schultheis et al. 2014). A comparison with the W_{CO} (peak) follows this tendency.

Among the three regions, the Chamaeleon region exhibits an intermediate H I and CO gas properties between the MBM 53–55 and Perseus regions. The lack of OB clusters in the Chamaeleon region yields relatively quiet environments, whereas low-mass star formations found in the CO cores may affect gas properties in the opaque regions.

Table 1. Physical quantities to represent gas properties of the MBM 53–55, Perseus, and Chamaeleon regions.

Region	τ_{353}	α	N_{H} [cm ^{−2}]	$\langle \tau_{\text{HI}} \rangle$	$\langle T_{\text{s}} \rangle$ [K]	$W_{\text{CO}}(\text{peak})$ [K km s ^{−1}]	$\langle X_{\text{CO}} \rangle$ [cm ^{−2} K ^{−1} km ^{−1} s]
MBM 53–55	$(7\text{--}600) \times 10^{-7}$	1.0	$(1\text{--}100) \times 10^{20}$	1.5	46	21	1.8×10^{20}
Perseus	$(3\text{--}800) \times 10^{-6}$	1.3	$(5\text{--}400) \times 10^{20}$	0.9	97	70	1.0×10^{20}
Chamaeleon	$(3\text{--}300) \times 10^{-6}$	1.2	$(6\text{--}200) \times 10^{20}$	1.3	62	25	1.4×10^{20}

The brackets indicate the average value for the parameters.

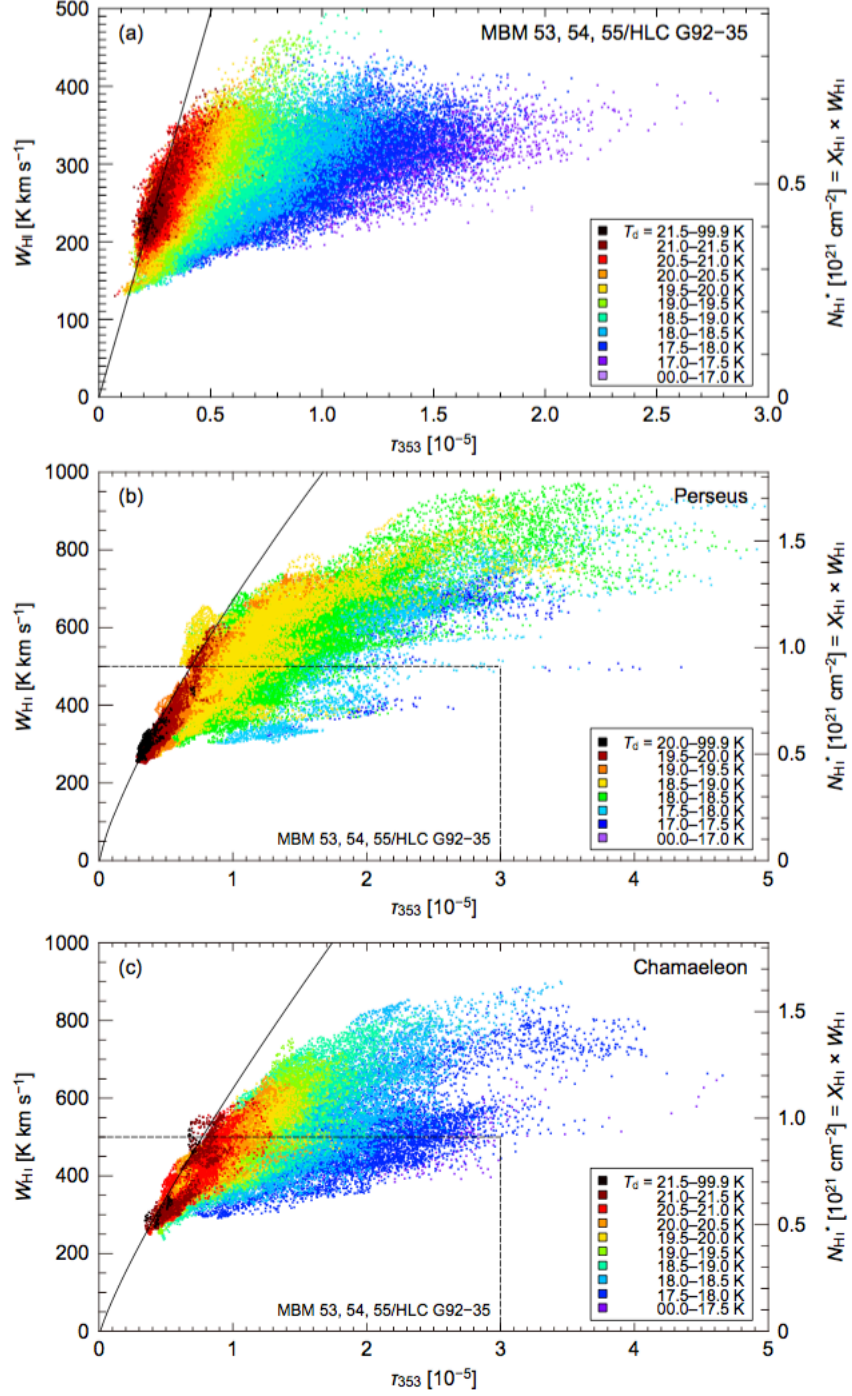


Figure 15. τ_{353} – W_{HI} correlation plots for the (a) MBM 53–55, (b) Perseus, and (c) Chamaeleon regions. The black solid line/curves indicate the W_{HI} theoretical model as a function of τ_{353} (Equation (7)) in the case of $\tau_{\text{HI}} \ll 1$, $\tau_{\text{HI}} = 0.21$ (see Appendix A in Okamoto et al. 2017), and 0.34 (see Appendix C) for the MBM 53–55, Perseus and Chamaeleon regions, respectively. For easier comparison, the horizontal and vertical ranges in the panel (a) are shown in the panels (b) and (c).

6. CONCLUSIONS

As part of an analysis of interstellar hydrogen gas based on the *Planck* data we carried out a comparative study of H I, CO and dust in the Chamaeleon molecular cloud complex. The main conclusions are summarized below.

1. A comparison of the J -band extinction A_J and submillimeter dust optical depth τ_{353} shows a relationship that τ_{353} increases as the ~ 1.2 th power of A_J . This indicates that the total column density N_H is modeled by the $\sim 1/1.2$ th power of τ_{353} , and suggests dust growth in dense molecular clouds. Similar trends are found in the Perseus and Orion A clouds, whereas the index may vary within about $\pm 10\%$ from region to region.
2. We have found a scatter correlation between τ_{353} and $W_{H I}$, similar to those found in the MBM 53–55 (F14) and Perseus (Okamoto et al. 2017) molecular cloud regions. Applying the nonlinear relation found in the τ_{353} – A_J relationship to the τ_{353} -based N_H model reproduces the scatter correlation, which indicates a large amount of the optically thick H I around the molecular clouds. The average $\tau_{H I}$ and T_s in the Chamaeleon region are derived to be ~ 1.3 and ~ 63 K, respectively.
3. A distribution of an X_{CO} factor in the Chamaeleon complex was derived. We have found variation of $X_{CO} \sim (0.5\text{--}3) \times 10^{20} \text{ cm}^{-2} \text{ K}^{-1} \text{ km}^{-1} \text{ s}$, which is consistent with the typical value in the Galaxy. This is possibly due to different physical conditions related to the surrounding ISRF.
4. Gas properties in the Chamaeleon region are compared with the MBM 53–55 and Perseus molecular cloud regions. The Chamaeleon region has moderate $\tau_{H I}$, T_s and X_{CO} among the three regions. The moderate ISRF in the diffuse medium and low-mass star-formation activities in the cores of clouds may relate to these gas properties.

This work was financially supported by Japan Society for the Promotion of Science (JSPS) KAKENHI, grant numbers 15H05694, 25287035. We acknowledge the use of the Legacy Archive for Microwave Background Data Analysis (LAMBDA), part of the High Energy Astrophysics Science Archive Center (HEASARC). HEASARC/LAMBDA is a service of the Astrophysics Science Division at the NASA Goddard Space Flight Center. The *Planck* satellite, an ESA science mission, is supported by ESA Member States, USA, and Canada. The CO data were obtained with the NANTEN telescope operated with a mutual agreement between Nagoya University and the Carnegie Institution of Washington. We also utilized all-sky H I map from the Parkes Galactic All-Sky Survey (GASS) and H α map (Finkbeiner 2003), combined with the data from Wisconsin H-Alpha Mapped (WHAM), Virginia Tech Spectral-Line Survey (VTSS) and Southern H-Alpha Sky Survey Atlas (SHASSA). The J -band infrared extinction map based on the NICEST method (Juvela & Montillaud 2016) and the 21 cm radio continuum map from CHIPASS (Calabretta et al. 2014) were also utilized in this study. Some of the results in this paper have been derived using the HEALPix (Górski et al. 2005) package.

Software: HEALPix (Gorski et al. 2005)

APPENDIX

A. HI GAS DISTRIBUTION SEPARATED IN VELOCITY

Figure 16 indicates HI velocity channel map from -40 km s^{-1} to $+20 \text{ km s}^{-1}$ separated into 5 km s^{-1} intervals, whose integrated intensities are averaged by the velocity range, which gives the HI brightness temperature (T_{HI}). These gas distributions exhibit roughly three structures,

- local clouds extensively distributed at $-5 \text{ km s}^{-1} \lesssim V_{\text{LSR}} \lesssim +10 \text{ km s}^{-1}$
- elongated gas structure, crossing the whole region around $b \sim -25^\circ$ at $-20 \text{ km s}^{-1} \lesssim V_{\text{LSR}} \lesssim -5 \text{ km s}^{-1}$ (IVA, see Planck Collaboration 2015)
- high velocity component located at $302^\circ \lesssim l \lesssim 314^\circ$ and $-30^\circ \lesssim b \lesssim -12^\circ$ seen at $V_{\text{LSR}} \lesssim -20 \text{ km s}^{-1}$.

In Figure 17, we give examples of the spectra showing these line profiles. The red and blue spectra have strong emissions from the IVA and the high velocity components. To avoid contamination from other than the local clouds, the IVA-dominated region at $l < 290^\circ$ and $b < -22^\circ$ and regions with the high velocity components are masked in the present study. Strong emission from the LMC outskirts detected at $+200 \text{ km s}^{-1} \lesssim V_{\text{LSR}} \lesssim +300 \text{ km s}^{-1}$ is also dropped by the mask (c) (see Figure 2).

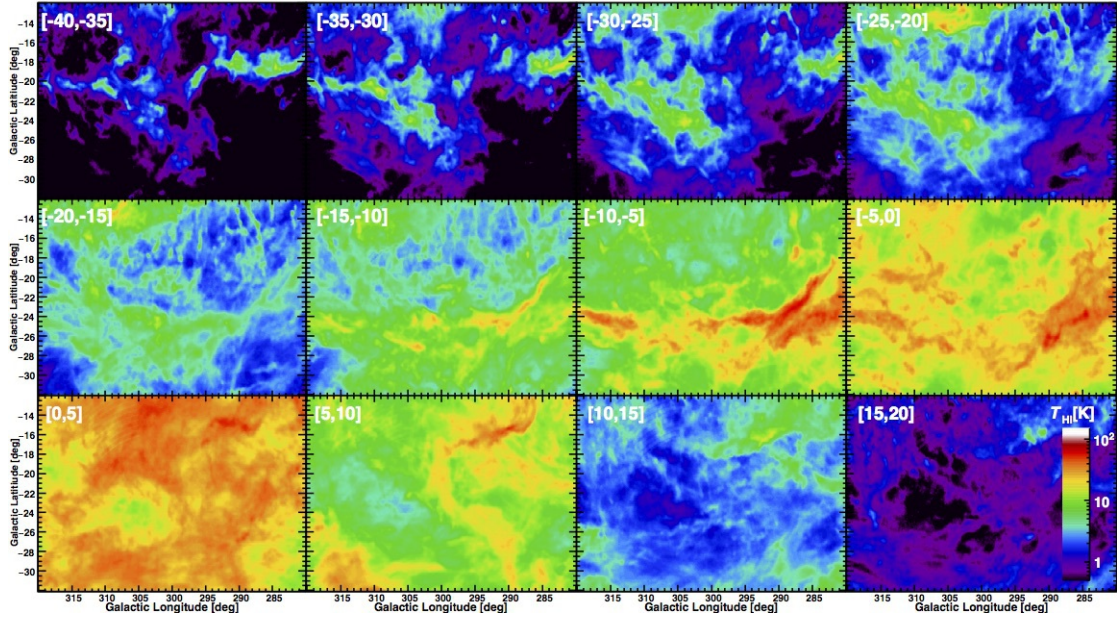


Figure 16. HI velocity channel distribution from -40 km s^{-1} to $+20 \text{ km s}^{-1}$, whose intensities are averaged within the velocity intervals of 5 km s^{-1} , giving the brightness intensity (T_{HI}) in units of K.

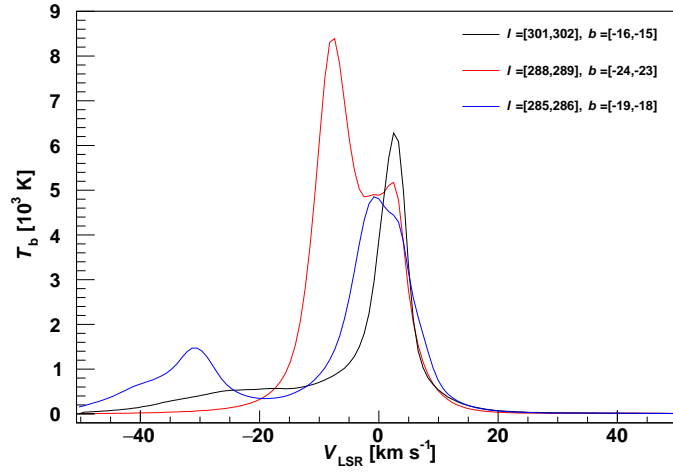


Figure 17. Examples of the H I line profiles for the three regions with size of $1^{\circ}0 \times 1^{\circ}0$, having the characteristic line profiles of the local (black), IVA (red) and the high velocity (blue) components. The brightness temperature (T_b) on the y-axis is a sum of T_b of each pixel. The regions with the red and blue spectra are included in the masked area.

B. CORRELATIONS OF W_{HI} AND W_{CO} WITH τ_{353}

We present correlations of W_{HI} and W_{CO} with τ_{353} sorted by T_d in Figures 18 and 19, respectively.

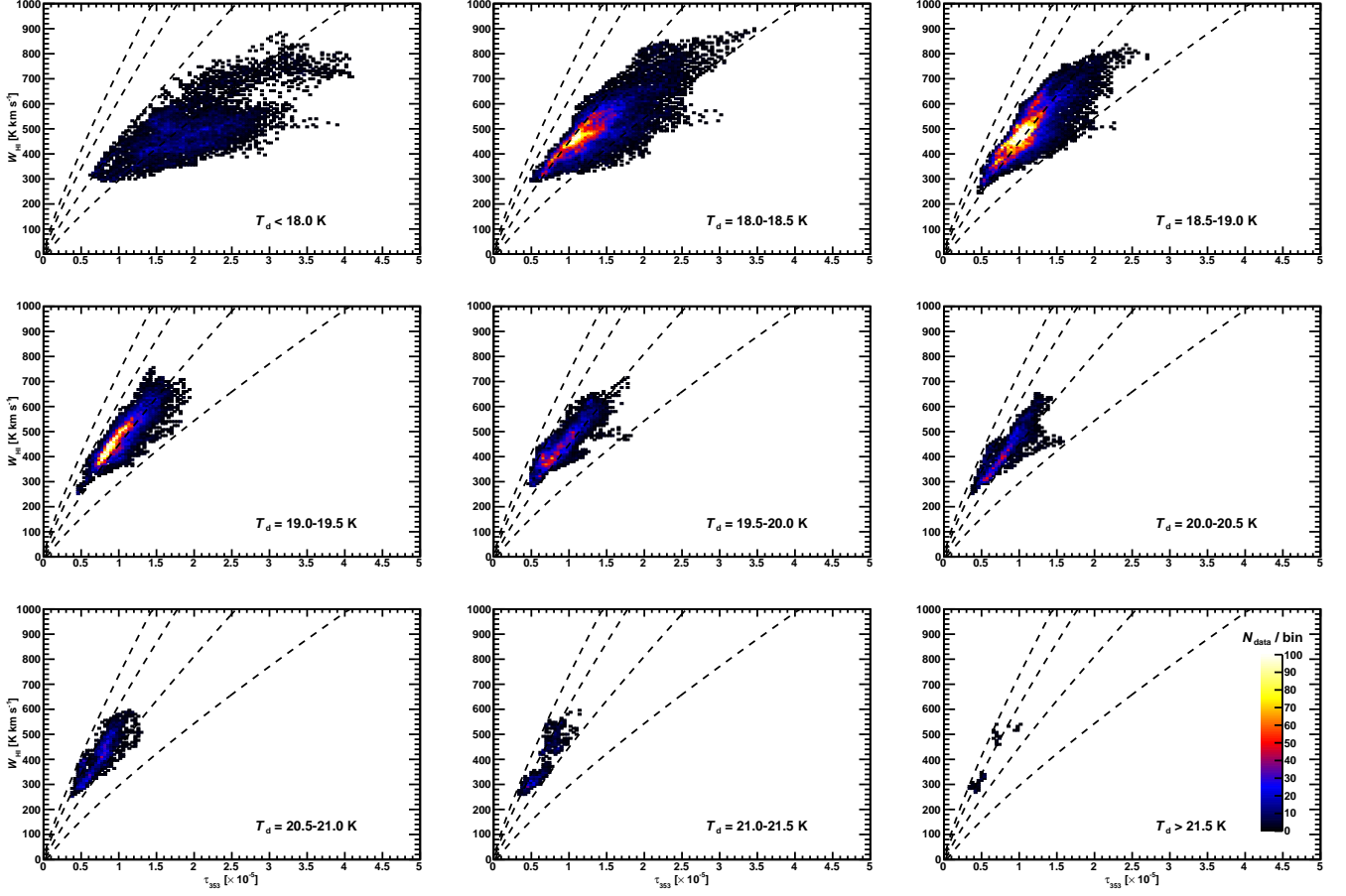


Figure 18. Correlation plots (in density) between τ_{353} and W_{HI} sorted by several T_d intervals. The dashed curves show the theoretical functions of Equation (7) for $\alpha = 1.2$, with $\tau_{\text{HI}} \ll 1$, $\tau_{\text{HI}} = 0.34$, 1.0 and 2.0 from left to right.

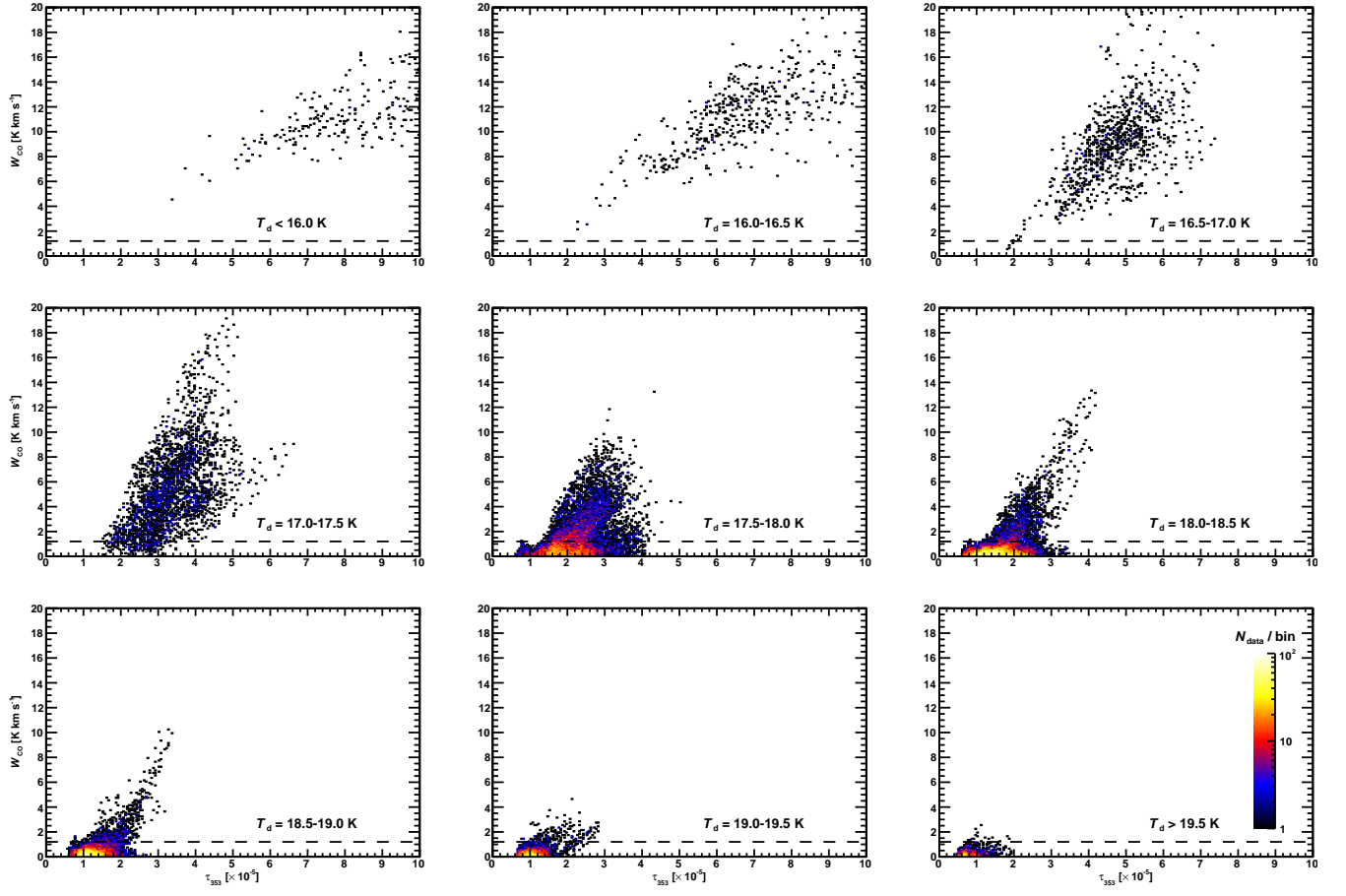


Figure 19. Correlation plots (in density) between τ_{353} and W_{CO} sorted by several T_d intervals. The horizontal dashed lines indicate 3σ confidence level in W_{CO} .

C. DERIVATION OF REFERENCE POINTS IN THE N_{H} MODEL

The reference points in the N_{H} model, $\tau_{353,\text{ref}}$ and $N_{\text{H,ref}}$ are determined in the same manner in Okamoto et al. (2017) for a study of the Perseus cloud. Figure 17(a) shows that a scatter plot between T_{d} and $\langle S_i \rangle$ (dispersion of each T_{d} interval in the $\tau_{353}-W_{\text{HI}}$ plot). The $\langle S_i \rangle$ is defined as a mean of the variance, which is derived from the areas of the right-angled triangles formed by each data point and regression line obtained by the fit to the data points in each T_{d} interval (cf., Figure 18 in Okamoto et al. 2017). As seen in the panel (a), the dispersion in T_{d} tends to become small with increasing T_{d} . The panel (b) represents a correlation between the averaged τ_{HI} ($\langle \tau_{\text{HI}} \rangle$) and $\langle S_i \rangle$ in each T_{d} for the MBM 53–55 region. We found a good positive correlation. By using this correlation as a template, τ_{HI} for the highest T_{d} in the Chamaeleon region is derived to be 0.34. Given a correlation, $N_{\text{H,ref}} = (1.15 \times 10^8) \times X_{\text{HI}} \times \tau_{353,\text{ref}}$, which is derived from the data points in the highest T_{d} for $-b- > 15^\circ$ in the all-sky data (F15), the model curve in Equation (7) with $\tau_{\text{HI}} = 0.34$ gives $\tau_{353,\text{ref}} = 7.8 \times 10^{-7}$ and $N_{\text{H,ref}} = 1.6 \times 10^{20} \text{ cm}^{-2}$, thorough the fit to the data points only for the highest T_{d} in the $\tau_{353}-W_{\text{HI}}$ relationship. Table 2 summarizes calculated dispersions in the $\tau_{353}-W_{\text{HI}}$ relationship for the Chamaeleon and MBM 53–55 regions.

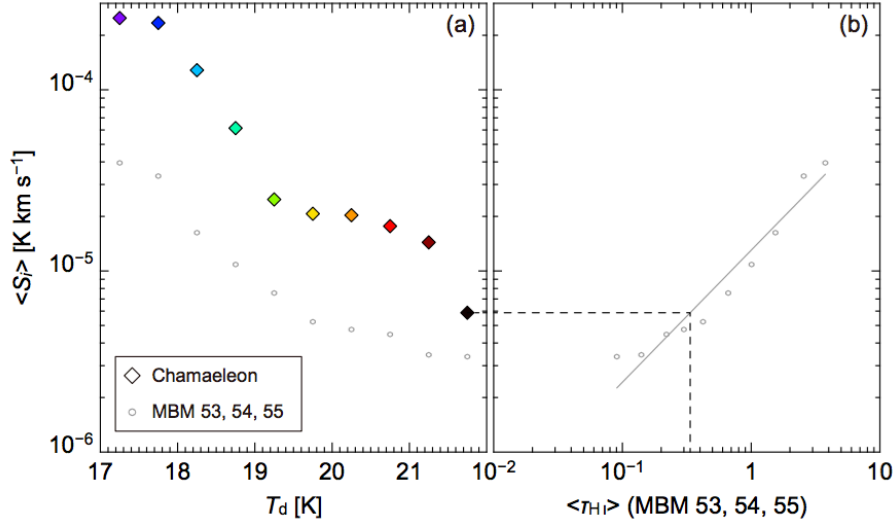


Figure 20. (a) Correlations between T_{d} and $\langle S_i \rangle$ (dispersion in the $\tau_{353}-W_{\text{HI}}$ relationship) for the MBM 53–55 and the Chamaeleon regions. For the Chamaeleon region, the data with different dust temperatures are shown by different colors adopted in Figure 15(c). $\langle S_i \rangle$ is defined as the mean area of the right-angled triangles formed by the data points and the regression line for each T_{d} intervals (Okamoto et al. 2017). (b) The template relationship between $\langle \tau_{\text{HI}} \rangle$ and $\langle S_i \rangle$ for the MBM 53–55 region. The solid line indicates the result of a linear regression. $\langle \tau_{\text{HI}} \rangle$ for the highest- T_{d} points in the Chamaeleon region can be estimated from $\langle S_i \rangle$ by using this template. The result gives $\langle \tau_{\text{HI}} \rangle = 0.34$.

Table 2. Dispersion of several T_d intervals in the τ_{353} – W_{HI} relationship for the Chamaeleon and MBM 53–55 regions.

T_d (K) (a)	Chamaeleon	MBM 53–55	
	$\langle S_i \rangle$ (10^{-5} K km s $^{-1}$) (b)	$\langle S_i \rangle$ (c)	$\langle \tau_{\text{HI}} \rangle$ (10^{-5} K km s $^{-1}$) (d)
21.5 j	0.09	0.59	0.34
21.0–21.5	0.14	1.44	0.34
20.5–21.0	0.22	1.77	0.45
20.0–20.5	0.30	2.03	0.48
19.5–20.0	0.42	2.07	0.52
19.0–19.5	0.66	2.48	0.76
18.5–19.0	1.01	6.14	1.09
18.0–18.5	1.54	12.8	1.63
17.5–18.0	2.56	23.4	3.34
j 17.5	3.76	24.9	3.95

(a) T_d range(b) Dispersions of each T_d for the (b) Chamaeleon region.

(c) The same as column (b) but for the MBM 53–55 region.

(d) HI optical depth $\langle \tau_{\text{HI}} \rangle$ for the MBM 53–55 region in each T_d (Table 3 in [Okamoto et al. 2017](#)).

D. X_{CO} DISTRIBUTION

We present the obtained X_{CO} maps with the different grid sizes in Figure 21.

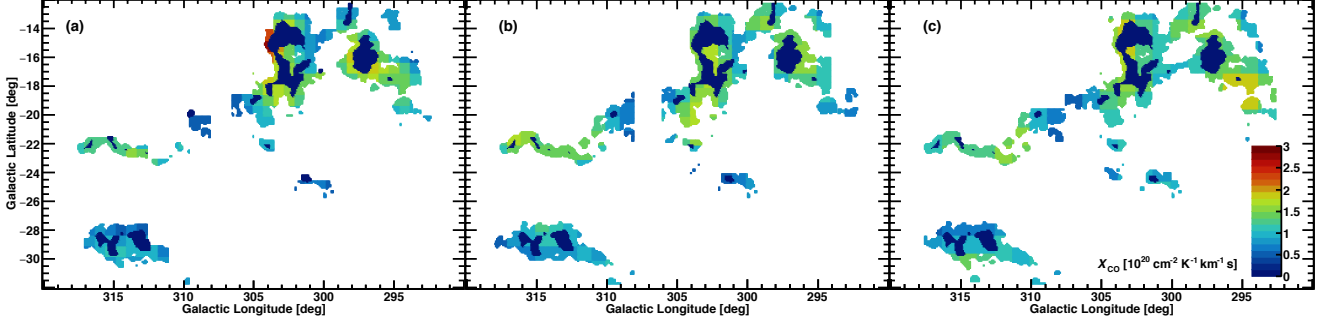


Figure 21. X_{CO} distribution derived from the correlation between W_{CO} and N_{H} (see Section 5.3): (a) 1.5×1.5 -based map smoothed with a two-dimensional Gaussian function with a kernel size of three pixels and $\sigma = 1^\circ$; (b) $2^\circ \times 2^\circ$ -based map with a Gaussian function of $\sigma = 1.3^\circ$; (c) 2.5×2.5 -based map with a Gaussian function of $\sigma = 1.7^\circ$. The grid sizes are (a) 0.75×0.75 , (b) 1.0×1.0 and (c) 1.25×1.25 .

REFERENCES

- Ackermann, M., Ajello, M., Allafort, A., et al. 2012b, *ApJ*, 755, 22
- Alcalá, J. M., Spezzi, L., Chapman, N., et al. 2008, *ApJ*, 676, 427
- Bally, J., Walawender, J., Johnstone, D., Kirk, H., & Goodman, A. 2008, *The Perseus Cloud*, ed. B. Reipurth, 308
- Bekhti, N., Flöer, L., Keller, R., et al. 2016, *A&A*, 594, A116
- Bell, T. A., Roue, E., Viti, S., & Williams, D. A. 2006, *MNRAS*, 371, 1865
- Bohlin, R. C., Savage, B. D., & Drake, J. F. 1978, *ApJ*, 224, 132
- Bolatto, A. D., Wolfire, M., & Leroy, A. K. 2013, *ARA&A*, 51, 207
- Boulanger, F., & Perault, M. 1988, *ApJ*, 330, 964
- Calabretta, M. R., Staveley-Smith, L., & Barnes, D. G. 2014, *PASA*, 31, e007.
- Case, G. L., & Bhattacharya, D. 1998, *ApJ*, 504, 761
- Cotten, D. L., & Magnani, L. 2013, *MNRAS*, 436, 1152
- Däppen, W. 2000, in *Allen's Astrophysical Quantities*, ed. A. N. Cox (4th ed.; New York: Springer), 27
- Dickey, J. M., Salpeter, E. E., & Terzian, Y. 1979, *ApJ*, 228, 465
- Dickey, J. M., & Lockman, F. J. 1990, *ARA&A*, 28, 215
- Dopita, M. A., & Sutherland, R. S. 2003, *Astrophysics of the Diffuse Universe* (Berlin: Springer)
- Draine, B. T. 2011, *Physics of the Interstellar and Intergalactic Medium*
- Finkbeiner, D. P. 2003, *ApJS*, 146, 407
- Fukui, Y., Okamoto, R., Yamamoto, H., et al. 2014, *ApJ*, 796, 59
- Fukui, Y., Torii, K., Onishi, T., et al. 2015, *ApJ*, 798, 6
- Fukui, Y., Hayakawa, T., Inoue, T., et al. 2018, *ApJ*, 860, 33
- Gerin, M., Liszt, H., Neufeld, D., et al. 2019, *A&A*, 626, A26
- Gillmon, K., Shull, J. M., Tumlinson, J., & Danforth, C. 2006, *ApJ*, 636, 891
- Górski, K. M., Hivon, E., Banday, A. J., et al. 2005, *ApJ*, 622, 759
- Glover, S. C. O., & Mac Low, M.-M. 2011, *MNRAS*, 412, 337
- Heiles, C., & Troland, T. H. 2003a, *ApJS*, 145, 329
- Heiles, C., & Troland, T. H. 2003b, *ApJ*, 586, 1067
- Heyer, M., & Dame, T. M. 2015, *ARA&A*, 53, 583
- Inoue, T., & Inutsuka, S.-i. 2012, *ApJ*, 759, 35
- Jones, A. P., Fanciullo, L., Kähler, M., et al. 2013, *A&A*, 558, A62
- Juvela, M., & Montillaud, J. 2016, *A&A*, 585, A38
- Kalberla, P. M. W., Burton, W. B., Hartmann, D., et al. 2005, *A&A*, 440, 775
- Kalberla, P. M. W., McClure-Griffiths, N. M., Pisano, D. J., et al. 2010, *A&A*, 521, A17
- Kalberla, P. M. W., & Haud, U. 2015, *A&A*, 578, A78

- Levrier, F., Le Petit, F., Hennebelle, P., et al. 2012, *A&A*, 544, A22
- Liszt, H. S., & Gerin, M. 2016, *A&A*, 585, A80
- Liszt, H. S., Gerin, M., & Grenier, I., 2018, *A&A*, 617, A54
- Lombardi, M., & Alves, J. 2001, *A&A*, 377, 1023
- Lombardi, M. 2009, *A&A*, 493, 735
- Martin, P. G., Roy, A., Bontemps, S., et al. 2012, *ApJ*, 751, 28
- McClure-Griffiths, N. M., Pisano, D. J., Calabretta, M. R., et al. 2009, *ApJS*, 181, 398
- Mizuno, A., Yamaguchi, R., Tachihara, K., et al. 2001, *PASJ*, 53, 1071
- Mizuno, T., Abdollahi, S., Fukui, Y., et al. 2016, *ApJ*, 833, 278
- Landsman, W. B. 1993, in *Astronomical Society of the Pacific Conference Series*, Vol. 52, *Astronomical Data Analysis Software and Systems II*, ed. R. J. Hanisch, R. J. V. Brissenden, & J. Barnes, 246
- Lee, M.-Y., Stanimirović, S., Wolfire, M. G., et al. 2014, *ApJ*, 784, 80
- Lombardi, M., & Alves, J. 2001, *A&A*, 377, 1023.
- Luhman, K. L. 2008, *Handbook of Star Forming Regions*, Vol. II, 169
- Okamoto, R., Yamamoto, H., Tachihara, K., et al. 2017, *ApJ*, 838, 132
- Ormel, C. W., Min, M., Tielens A. G. G. M., et al. 2011, *A&A*, 532, A43
- Ossenkopf, V., & Henning, T. 1994, *A&A*, 291, 943
- Pineda, J. E., Caselli, P., & Goodman, A. A. 2008, *ApJ*, 679, 481
- Planck Collaboration XIX, 2011, *A&A*, 536, A19
- Planck Collaboration, Abergel, A., Ade, P. A. R., et al. 2011b, *A&A*, 536, A24
- Planck Collaboration XI, 2014a, *A&A*, 571, A11
- Planck Collaboration XIII, 2014b, *A&A*, 571, A13
- Planck Collaboration XVII, 2014c, *A&A*, 566, A55
- Planck Collaboration XXVIII, 2015, *A&A*, 582, A31
- Remy, Q., Grenier, I. A., Marshall, D. J., et al. 2018, *A&A*, 611, A51
- Roy, A., Martin, P. G., Polychroni, D., et al. 2013, *ApJ*, 763, 55
- Smith, R. J., Glover, S. C. O., Clark, P., et al., 2014, *MNRAS*, 441, 1628
- Stanimirović, S., Murray, C. E., Lee, M.-Y., et al. 2014, *ApJ*, 793, 132
- Schlegel, D. J., Finkbeiner, D. P., & Daris, M. 1998, *ApJ*, 500, 525
- Schultheis, M., Chen, B. Q., Jiang, B. W., et al. 2014, *A&A*, 566, A120
- Wolfire, M. G., Hollenbach, D., & McKee, C. F. 2010, *ApJ*, 716, 1191
- Yamamoto, H., Onishi, T., Mizuno, A., & Fukui, Y. 2003, *ApJ*, 592, 217.
- Ysard, N., Köhler, M., Jones, A., et al. 2015, *A&A*, 577, 110